Electronic Supplementary Information

Solar-driven CO_2-to-ethanol conversion enabled by continuous CO_2 transport via a superhydrophobic Cu_2O nano fence

Hailing Huo, [a] Hua He, [b] Chengxi Huang, [a] Xin Guan, [b] Fang Wu, [c] Yongping Du, [a] Hongbin Xing, [a] Erjun Kan,*[a] and Ang Li*[a]

a H. Huo, Prof. C. Huang, Dr. Y. Du, H. Xing, Prof. E. Kan, Prof. A. Li
MIIT Key Laboratory of Semiconductor Microstructure and Quantum Sensing, School of Science
Nanjing University of Science and Technology
Nanjing 210094, P. R. China
E-mail: liang2100@njust.edu.cn
ekan@njust.edu.cn

b H. He, X. Guan
State Key Laboratory of Heavy Oil Processing and College of Chemical Engineering
China University of Petroleum (East China)
Qingdao 266580, P. R. China.

c Prof. F. Wu
College of Information Science and Technology
Nanjing Forestry University
Nanjing 210037, P. R. China.

Contents

Experimental Procedures

Chemicals

Copper chloride ($CuCl_2 \cdot 2H_2O$, AR), copper bromide ($CuBr_2$, AR), copper sulfate ($CuSO_4 \cdot 5H_2O$, AR), tetrabutylammonium bromide ($(C_4H_9)_4NBr$, AR), ascorbic acid (AR), 1-dodecanethiol ($C_{12}H_{25}$-SH, 99.5%), scopoletin ($C_{10}H_8O_4$, 98%), and horseradish peroxidase (≥ 500 units/mg) were purchased from Aladdin. Copper nitrate ($Cu(NO_3)_2 \cdot 3H_2O$, AR) and potassium bicarbonate ($KHCO_3$, AR) were purchased from Macklin. Sodium hydroxide (NaOH, AR), ethanol (C_2H_5-OH, AR), silver nitrate ($AgNO_3$, >99.0%), and ammonium sulfate ($(NH_4)_2SO_4$, AR) were purchased from Sinopharm Chemical Reagent Co., Ltd. Polyvinylpyrrolidone (PVP, M.W = 30000) was purchased from Shanghai Yuanye Bio-Technology Co., Ltd. Dimethyl sulfoxide (DMSO) was purchased from Sigma-Aldrich. Cy5 NHS ester was purchased from Shanghai So-Fe Biomedicine Co., Ltd. Nafion® D520 dispersion was purchased from 3AMaterials®. Deionized water (DI water, 18.25 MΩ·cm) obtained from a UP Water Purification System was used throughout the experimental processes. All chemicals were obtained from commercial suppliers and used without further purification.

Sample preparation

Synthesis of Cu_2O hollow sphere (CHS). An aqueous solution was first prepared by mixing 20 mL of DI water, 0.4 mL of PVP solution (M.W = 30000, 1.0 wt %), 2.0 mL of $(C_4H_9)_4NBr$ solution (0.1 M), and 0.2 mL of $CuCl_2$ solution (0.1 M). Then 1.0 mL of ascorbic acid solution (0.1 M) was added to the solution. The mixture was stirred for 3 min and became turbid shortly. Afterwards, 1.0 mL of NaOH solution (0.2 M) was added to the above turbid precursor solution under stirring, and the resulting solution was then kept for 15 min at room temperature without stirring. The resultant Cu_2O product was collected through centrifugation, washed with DI water and ethanol several times, and finally dried in a vacuum oven.

Synthesis of Cu_2O solid sphere (CSS). 28.6 mg of $Cu(NO_3)_2 \cdot 3H_2O$ and 57.8 mg of $(NH_4)_2SO_4$ were added to 50 mL of DI water and stirred for 5 min. Then 2.0 mL of a 0.2 M NaOH solution was dropwise injected into the above solution and stirred magnetically for 2 min, followed by the dropwise addition of 3.5 mL of ascorbic acid (0.1 M). Finally, the solution was stirred for an additional 13 min. The resultant Cu_2O product was collected through centrifugation, washed with DI water and ethanol several times, and finally dried in a vacuum oven.

Synthesis of Cu_2O nanosheets derived from fragmented CHS (CNS). The synthetic process of CNS was similar to that of CHS. The difference was that the standing time was extended from 15 min to 45 min.

Surface modification to synthesize superhydrophobic Cu_2O structures. The as-prepared Cu_2O samples of CHS, CSS, and CNS were all treated with 1-dodecanethiol (DDT) to obtain superhydrophobic samples. The resulting superhydrophobic Cu_2O structures were denoted as O-CHS, O-CSS, and O-CNS, respectively. In a typical procedure, 10 mg of Cu_2O was ultrasonically dispersed in 10 mL of ethanol, followed by the injection of 7 μL of DDT. The mixture was then gently stirred at room temperature for 15 min. The resultant superhydrophobic Cu_2O was collected through centrifugation, washed with ethanol several times, and finally dried in a vacuum oven.

Instrumentation

Transmission electron microscope (TEM) was performed using a JEOL JEM 2100F electron microscope. Scanning electron microscope (SEM) was performed on Hitachi SU8220. Crystalline structures were evaluated by X-ray diffraction (XRD) analysis using a Bruker D8 Focus operating at 40 kV and 40 mA, equipped with a nickel-filtered Cu Kα radiation (λ = 1.54056 Å). Specific surface areas and pore structures of catalysts were measured using Micromeritics ASAP 2460 through nitrogen adsorption at 77 K. The specific surface areas were calculated from the isotherms using the BET method. The pore distribution was obtained by the BJH method from the adsorption branch of the adsorption isotherms. Room temperature steady-state photoluminescence (PL) spectra were performed on FL 970 fluorescence spectrophotometer under the excitation wavelength of 350 nm with a 510 nm filter.

Time-resolved PL spectra were performed on a HITACHI F-7100 fluorescence spectrophotometer under an excitation wavelength of 350 nm. UV-vis diffuse reflectance spectra were recorded using UV-2600 under the visible light of 400-800 nm. Reflectivity was used to measure light absorption through the conversion of the Kubelka-Munk formula, and $BaSO_4$ was used as the reference sample. X-ray photoelectron spectroscopy (XPS) was performed on Thermo Fischer, ESCALAB 250Xi with Al K X-ray source to reveal chemical states, and the binding energies (BE) were calibrated using the C 1s electron peak (BE = 284.8 eV). Raman spectra were recorded using Raman spectrometer DXR2. In situ Fourier transform infrared spectroscopy (FTIR) spectra were performed on Thermo Fisher Nicolet IS50. Water contact angles were measured using an SDC-350 instrument with the samples uniformly dispersed on glass substrates using ethanol as solvent. The volume of the water droplet was 7 μL, and the final results were average values obtained from more than three positions. Total internal reflection fluorescent microscope (TIRFM) measurements were carried out on Nikon A1.

Supplementary tests

Ag^+ probe experiment. Ag^+ probe experiments were conducted to confirm that the hydrophobic treatment did not hinder the migration of charge carriers to the catalyst surface. Ag^+ (derived from $AgNO_3$) and methanol were used as the probe ion and positive charge scavenger, respectively. Typically, 15 mg of catalysts (O-CHS or CHS) was dispersed in 30 mL of H_2O. Then 15 mL of methanol and 250 μL of $AgNO_3$ solution (20 mg mL^{-1}) were added. After stirring and evacuation for 0.5 h, the mixture was irradiated with a 300 W Xe lamp (λ > 420 nm) for 3 h. The Ag-loaded catalyst was obtained after centrifugation, washing, and drying procedures. During the experiment, Ag^+ would be reduced to Ag particles by the photogenerated electrons migrating to the catalyst surface. Therefore, by comparing the amount of deposited Ag on O-CHS and CHS, the amount of photogenerated electrons transferred to the catalyst surface can be compared.

Photoelectrochemical measurement. Photoelectrochemical measurements were conducted using a CHI-660E electrochemical workstation from China. The measurements were performed in a standard three-electrode configuration, with the prepared samples serving as the working electrode, a platinum plate as the counter electrode, and the standard Ag/AgCl electrode as the reference. A 0.2 M Na_2SO_4 aqueous solution was used as the electrolyte. The working electrode was prepared as follows: 8 mg catalyst was dispersed in 2 ml of H_2O, 2 ml of isopropanol, and 190 μL of Nafion® D520 dispersion. Then 100 μL of the aforementioned mixture was dropped onto an FTO glass with an area of 1 cm^2. The photocurrent of the samples was measured under a 300 W Xe lamp (PLS-SXE300, PerfectLight, China) irradiation equipped with a 420 nm cutoff filter. The light on/off cycle was set to 10 s. Electrochemical impedance spectroscopy (EIS) was conducted in a frequency range from 0.1 Hz to 100 kHz.

Total internal reflection fluorescent microscope measurement. Total internal reflection fluorescence microscope (TIRFM) measurements were carried out on Nikon A1. The specific procedure was as follows. Firstly, Cy5 NHS ester was dissolved in DMSO with a concentration of 85 mM. Then 1 μL of Cy5 NHS ester solution (85 mM in DMSO) was added to 2 mL of H_2O to form aqueous solution A. Moreover, 5 mg of catalyst was dispersed into 1 mL of H_2O, and then 10 μL of solution A was added to form solution B. After that, solution B was wrapped in tinfoil to avoid exposure to light and placed in the refrigerator overnight. Afterwards, 100 μL of the obtained solution B was dropped on a cleaned coverslip. After 2 h, the coverslip was placed on the TIRFM for imaging using direct stochastic optical reconstruction microscopy with an excitation of 635 nm.

Calculation of the infiltration pressure required for water to penetrate the pores. To verify the nano-fence effect of O-CHS, the pressure-driven infiltration behavior of water into the catalyst's pores was investigated. The applicability of the Young-Laplace (Y-L) equation has been demonstrated to be valid in the nanoscale regime, rendering it a widely accepted tool for describing capillary pressure phenomena associated with pore sizes at the nanoscale level.[1, 2] Accordingly, the infiltration pressure is calculated using the Y-L equation, expressed by equation (1).[3]

$$\Delta P = P_{\text{interior}} - P_{\text{exterior}} = 2\gamma / \mathrm{R} \quad (1)$$

where P_{interior} and P_{exterior} represent the pressure on the inner and outer sides of the liquid surface in the pore, respectively. ΔP refers to the Laplace pressure (infiltration pressure), which is the pressure difference across the liquid interface. γ is the surface tension of the liquid and R is the radius of curvature of the liquid surface.

For the hydrophobic material ($\theta > 90°$), as illustrated in Fig. S16a to S16c, water advancing inside the pore will form a convex liquid surface due to its surface tension. In this case, the direction of ΔP_1 is from the gas phase to the liquid phase, preventing water from entering the pores. Moreover, R = a / sin(θ-90°). Here, a is the radius of the pore and θ is the contact angle that the liquid makes on the sidewall of the pore. For the hydrophilic material ($\theta < 90°$), as illustrated in Fig. S16d to S16f, water advancing inside the pore will form a concave liquid surface. In this case, the direction of ΔP_2 is from the liquid phase to the gas phase, pushing water into the pores. Moreover, R = a / cosθ.

In this study, γ is approximated by the surface tension of water, which is 74.92 mN m^{-1} at the photoreaction temperature of 5 °C.[4] θ is approximated by the water contact angle of the catalyst. For O-CHS with θ of 152.24°, $\Delta P_1 = 2\gamma \sin(\theta\text{-}90°) / a$. Whereas for CHS with θ of 43.96°, $\Delta P_2 = 2\gamma \cos\theta / a$. Consequently, the infiltration pressure is inversely proportional to pore size.

CO_2 photoreduction test. The performance of catalysts for overall PCRR were evaluated using Labsolar 6A (PerfectLight, China) and gas chromatography (GC, Agilent 8890, America).

Prior to illumination, 20 mg of catalysts was added to 100 mL of $KHCO_3$ (0.1 M) aqueous solution without using hole scavengers. The mixture was magnetically stirred in a double-layer Pyrex glass reactor (PerfectLight, China). The superhydrophobic catalysts would float on the aqueous solution, while a suspension would form for the hydrophilic catalysts. The reactor was then connected to Labsolar 6A, constituting the system for photoreduction tests (Fig. S18a to S18c). Then the system was evacuated to 0.5 kPa. Subsequently, compressed CO_2 (99.999%), which was controlled by a mass flow controller (LZB-3WB, China), was bubbled into the reactor to raise the system pressure to 80 kPa. The system was then evacuated again. This extraction-inflation operation was repeated three times to remove as much air as possible. Finally, pure CO_2 was continuously bubbled through the solution again at a 40 mL min^{-1} flow rate for approximately 30 min to raise the CO_2 pressure to 80 kPa under constant stirring at 250 r min^{-1}. Then the system was maintained for 40 min to reach CO_2 dissolution equilibrium. The extraction-inflation and dissolution processes are schematically shown in Fig. S18d to S18g. No additional CO_2 was injected into the closed system during the reaction. A 300 W Xe lamp (PLS-SXE300, PerfectLight, China) equipped with a 420 nm cutoff filter was then used as the visible light source through the quartz window. The distance between the light source and the quartz window was kept constant at 10 cm. The photoreaction temperature was maintained at 5 °C using a chiller (CNSHP DC-0506, China) for cooling water circulation. The reaction was typically conducted for 6 h, and 0.5 mL of liquid products was taken out using a syringe every hour for subsequent analysis. Comparative experiments were carried out under the similar experimental conditions.

The amounts of gaseous and liquid products evolved were all determined using GC. Gas products were directly detected by GC, which was equipped with a thermal conductivity detector (TCD), a flame ionization detector (FID), and a methanation reactor. For liquid products, the samples obtained at each hour were injected into GC through a headspace sampler (APL HS-20, China) for analysis. Specifically, 200 μL of the extracted liquid was mixed with 5 mL of H_2O in each headspace bottle, and then the bottle was placed into the headspace sampler. The liquid products were automatically injected into the GC for detection. An external standard was used to calculate the amount of each component based on the peak area of GC.

Careful calculation is required to determine the amount of O_2. The presence of a potential air leak during the reaction introduces the possibility of O_2 from the ambient air entering the reaction system, leading to inaccuracies in determining the generated O_2 content. To mitigate this error, calibration was performed by comparing the O_2 content generated from the reaction with the N_2 content, allowing for the accurate determination of the actual amount of generated O_2. Specifically, as N_2 cannot be generated from the overall PCRR, the detection of N_2 in the GC signifies its origin as air leakage. Considering a volume ratio of 20.9: 78.1 for O_2 to N_2 in ambient air, the quantity (mL) of O_2 resulting from air leakage can be determined based on the corresponding volume (mL) of N_2. Consequently, the volume (mL) of O_2 generated by the reaction can be obtained by subtracting the volume (mL) of O_2 caused by air leakage.

$Cu(OH)_2$ probe experiment. To further verify the nano-fence effect of O-CHS to prevent water from entering the hollow space, the $Cu(OH)_2$ precipitate was used as the probe for O-CHS and CHS. Typically, 10 mg of the catalyst was dispersed in 10 mL of H_2O. Then, 200 μL of $Cu(SO_4)_2$ solution (0.2 M) was added, followed by stirring for 0.5 h to allow complete entry of Cu^{2+} into the interior of the catalyst through the pores. Next, 200 μL of NaOH solution (1 M) was added, resulting in the formation of blue

flocculent precipitates, namely $Cu(OH)_2$. After 5 min of stirring, the resultant sample was collected through centrifugation, and subsequently washed multiple times with H_2O and ethanol. During this experiment, if Cu^{2+} ions are able to permeate the interior of the hollow structure of catalysts through the pores with the aqueous solution, the addition of NaOH solution would cause the formation of precipitated particles both inside and outside the hollow structure. After the centrifugal washing process, the precipitated particles outside the hollow structure would be removed, while those within the hollow structure would be retained. Conversely, if the aqueous solution fails to penetrate the interior of the hollow structure, Cu^{2+} will not be able to enter, resulting in the absence of precipitation particles inside the hollow structure. Consequently, the presence or absence of precipitated particles inside the hollow structure can serve as an indicator for determining the permeability of water into the internal region of the hollow structure.

CO_2 dissolution rate test. To verify that the dissolution rate of CO_2 in aqueous solutions with hydrophobic catalysts is more favorable compared to systems with hydrophilic catalysts, the temperature and pressure changes of the photoreduction measurement system during the dissolution of CO_2 (Fig. S18g) were recorded in detail. The recorded data was then used to calculate the quantities of CO_2 present in both the gas and liquid phases of the system at different dissolution times. As described in ***CO_2 photoreduction test*** and Fig. S18, the system underwent several processes of extraction and inflation. Consequently, during the dissolution of CO_2, the pressure value displayed on the Labsolar 6A actuator (Fig. S18b) was the real-time CO_2 pressure in the gas phase of the system. Thus, if the change of pressure and temperature over time during CO_2 dissolution could be recorded, the change in the amount of CO_2 in the gas phase could be calculated using the van der Waals equation. Since the system was composed of Labsolar 6A and a reactor, the temperatures of the two parts were not the same. Therefore, the system should be divided into two parts to calculate. For Labsolar 6A, the corresponding temperature was displayed on the actuator (Fig. S18b). While for the reactor (Fig. S18c), the temperature was maintained constant at 5 °C through cooling water circulation. Notably, during the testing process, we maintained strict control over several parameters. The quantity of catalyst employed remained constant at 20 mg, while the rate at which CO_2 was introduced into the system was fixed at 40 mL min^{-1}. To measure and regulate this gas flow, we utilized a mass and volumetric gas flow meter from Omega (model FMA-1604A). Additionally, we ensured that the stirring speed was set at a constant rate of 250 r min^{-1} by utilizing a magnetic stirrer manufactured by JOANLAB (model MS-10L). Furthermore, we maintained a consistent temperature of 5 ℃ for the solution in the reactor by employing a chiller (CNSHP DC-0506, China) to circulate cooling water. By carefully controlling these external factors, we aimed to eliminate their potential influence on the experimental outcomes. The van der Waals equation is expressed as equation (2):

$$(P + n^2a / V^2)(V - nb) = nRT \quad (2)$$

where P is the pressure of the system displayed on the Labsolar 6A actuator. n is the amount of CO_2 in the gas phase. V is the volume of gas. R is the molar gas constant. T is the temperature. a and b are the van der Waals constants. For CO_2, a = 0.3658 $Pa \cdot m^6\ mol^{-2}$, $b = 0.429 \times 10^{-4}\ m^3 \cdot mol^{-1}$. n is calculated using Mathematica software.

For the part of Labsolar 6A, V_1 is 100 mL, and P_1 and T_1 are both displayed on the actuator. For the part of the reactor, the total volume of the reactor is 370 mL, but the aqueous solution occupies a volume of 100 mL. Thus, the volume occupied by CO_2 in the gas phase of the reactor (V_2) is 270 mL. Furthermore, T_2 for this part is 5 °C. Since the pressure of the system is in equilibrium, P_2 is equal to P_1. The sum of corresponding n_1 and n_2 is the total amount of CO_2 in the gas phase. Hence, the total amount of CO_2 in the gas phase at different dissolution times can be calculated. The decrease in the total amount of CO_2 in the gas phase corresponds to the amount of CO_2 dissolved into the liquid phase. Thus, the relationship between the amount of CO_2 dissolved into the liquid phase and its dissolution time can be obtained, and that is the dissolution rate of CO_2.

Calculation of selectivity. The selectivity from the overall PCRR on an electron basis ($6e^-$ for CH_3OH, $12e^-$ for CH_3CH_2OH, $2e^-$ for H_2) was calculated using equations (3) and (4):

$$\text{Selectivity of carbon derivatives (\%)} = (6\,n_{methanol} + 12\,n_{ethanol}) \times 100\% / (6\,n_{methanol} + 12\,n_{ethanol} + 2\,n_{hydrogen}) \quad (3)$$

$$\text{Selectivity of ethanol (\%)} = 12\,n_{ethanol} \times 100\% / (6\,n_{methanol} + 12\,n_{ethanol} + 2\,n_{hydrogen}) \quad (4)$$

where $n_{methanol}$, $n_{ethanol}$, and $n_{hydrogen}$ represent the amounts (moles) of methanol, ethanol, and hydrogen formed within a certain period of time, respectively.

Calculation of solar-to-ethanol conversion efficiency. The solar-to-ethanol conversion efficiency (STE) can be quantified as the ratio of the chemical energy output for ethanol production to the solar energy input. It can be calculated using equation (5):[5-7]

STE (%) = Output energy for ethanol evolved × 100% / Energy of incident solar light (5)

This equation can be further expanded as:

STE (%) = $R_{ethanol}$ (μmol h^{-1}) × ΔG_r (kJ mol^{-1}) × 100% / $P_{average}$ (mW cm^2) × S (cm^2)

where $R_{ethanol}$ indicates the rate of ethanol formation during the overall PCRR. ΔG_r represents the Gibbs energy change for the CO_2-to-ethanol reaction. $P_{average}$ is the average irradiation intensity, and S is the incident irradiation area. For this study, S is determined to be 38.465 cm^2.

The irradiation intensity of the 300 W Xe lamp with a cutoff 420 filter was measured using a CEL-FZ-A Optical Power Meter. Five different test positions (Fig. S22) were adopted to determine the average irradiation intensity $P_{average}$, and it was found to be 125.58 mW cm^{-2}, following equation (6).[8]

$$P_{average} = P_{center} / 3 + 2P_{edge} / 3 \quad (6)$$

The reaction Gibbs energy change ΔGr can be calculated using equation (7):

$$\Delta G_r = \sum \nu_i \Delta_f G_i \quad (7)$$

where i is the stoichiometric coefficient for species i in the formation reaction. $\Delta_f G_i$ is the molar Gibbs energy of formation for species i. In this study, the overall PCRR conditions are approximated as standard states, and the thermodynamic data used are summarized in Table S10.[4]

Considering the CO_2-to-ethanol reaction with the chemical formula: $2CO_2 + 3H_2O \rightarrow CH_3CH_2OH + 3O_2$

Thus, ΔG_r can be calculated as follows:

$$\Delta G_r = \Delta_f G_{ethanol}^{\Theta} + 3\Delta_f G_{oxygen}^{\Theta} - 2\Delta_f G_{carbon\ dioxide}^{\Theta} - 3\Delta_f G_{water}^{\Theta}$$

$$= (-174.8)\ kJ\ mol^{-1} - 2 \times (-394.4)\ kJ\ mol^{-1} - 3 \times (-237.1)\ kJ\ mol^{-1} = 1325.3\ kJ\ mol^{-1}$$

Combining the value of $R_{ethanol}$ (996.18 μmol g^{-1} h^{-1} × 0.02 g = 19.92 μmol h^{-1}), the STE was calculated to be 0.152%.

Isotope-labeling test. The isotope labeling experiment was conducted as follows. Firstly, 30 mg of O-CHS was added to 50 mL of $NaH^{13}CO_3$ (0.1 M) solution in the reactor for ultrasonic dispersion. Subsequently, the reactor was connected to Labsolar 6A, sealed, and purged with flowing Ar for 60 min to remove air. Afterwards, $^{13}CO_2$ (99.999%) was introduced into the reactor, raising the final pressure for the reaction to 80 kPa. The reactor was allowed to stabilize for 40 min, after which the overall PCRR was performed for 4 h using a 300 W Xe lamp with a cutoff 420 filter. The products containing C-isotopes were analyzed by GC-MS (Shimadzu QP-2010SE).

Detection of hydrogen peroxide (H_2O_2) in the reaction solution. The detection of H_2O_2 in the reaction solution was conducted through a chemiluminescence approach by scopoletin assay.[9, 10] Firstly, the detection solution was prepared by mixing 20 mL of H_2O, 5 mL of HCl (0.1 M), 500 μL of scopoletin solution (0.7 mg L^{-1}), and 1 mL of horseradish peroxidase solution (0.16 mg mL^{-1}). Subsequently, 10 mL of the reaction solution obtained after the overall PCRR with different catalysts was added to the detection solution. After incubation for 15 min, the final solution was measured using a fluorescence spectrophotometer with excitation of 350 nm light. A reference experiment was conducted in the same manner, except that 10 mL of H_2O was added instead of the reaction solution.

In situ Fourier-transform infrared spectroscopy (FTIR) test. Diffuse reflection in situ FTIR was used to investigate effective CO_2 adsorption on the catalyst surface and detect possible intermediates during the overall PCRR. 50 mg of the catalyst was loaded onto the sample cell of the diffuse reflectance attachment, ensuring a flat top surface. A cover was fixed on the sample holder to form a reaction space, which was then cleaned by Ar. Then the FTIR data was collected as the background. Subsequently, visible light was introduced into the reaction space through the observation window, and CO_2 was introduced via a container. It should be noted that the container was filled with water to ensure the formation of a water film on the sample powders. FTIR data was collected every 10 min to monitor and record any changes.

Computational details.

All optimized geometries and electronic energies based on the spin-polarized density functional theory (DFT) were performed using the Vienna *ab initio* simulation package. The exchange-correlation function was treated within the generalized gradient approximation (GGA) and parameterized by the Perdew-Burke-Ernzerhof (PBE) formula to describe the electronic exchange and correlation effects. Van der Waals interactions were described using the empirical correction in Grimme's scheme (DFT-D3). The cutoff energy for the plane wave basis sets was set to 500 eV, and the Methfessel-Paxton (width = 0.1 eV) was used to calculate the partial occupancies. A vacuum layer with a thickness of 20.00 Å was placed along the vertical direction to avoid spurious interactions. The Brillouin zone integration was performed using a Monkhorst-Pack special k-points mesh of 3×3×1 for all the calculation models. The Cu_2O (111) surface was constructed, and a 3×3 supercell with three layers was selected as the computational model. During the optimization, the atoms in the bottom two layers were fixed to maintain the bulk structure, while the other atoms in the top layer were allowed to fully relax.

Results and Discussion

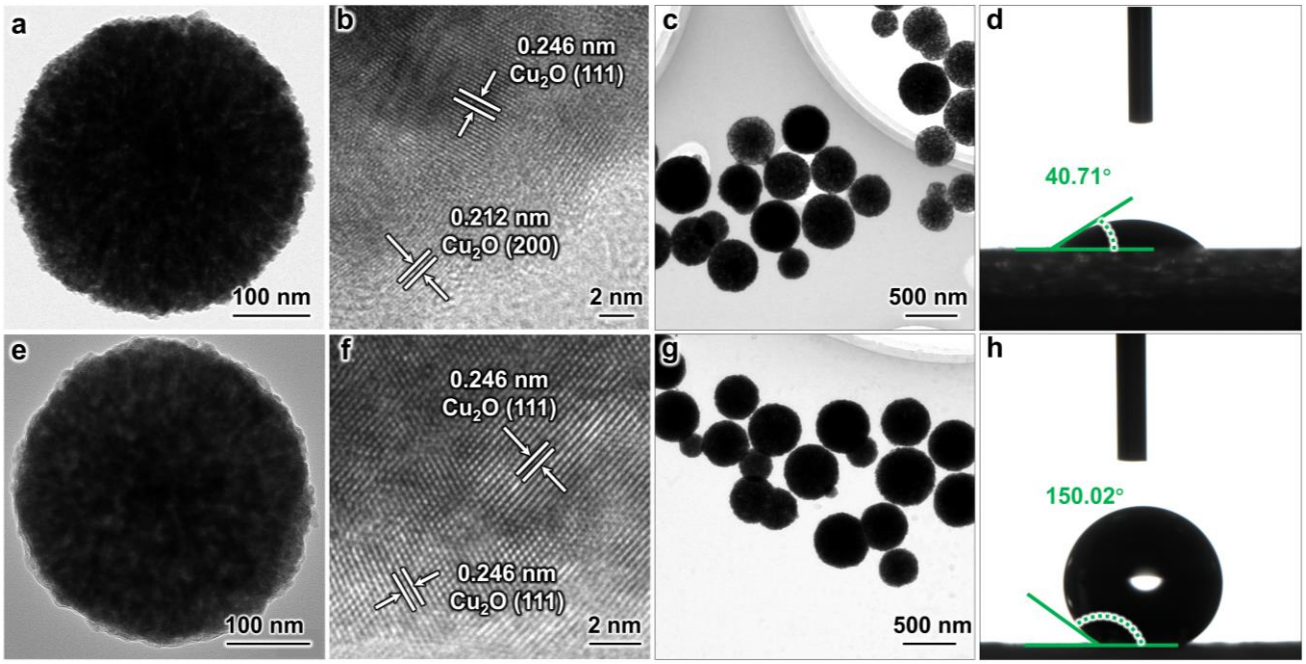

Fig. S1 Morphologies and wettability of CSS and O-CSS. (a, c) TEM images of CSS. (b) HRTEM image of CSS. (d) WCA of CHS. (e, g) TEM images of O-CSS. (f) HRTEM image of O-CSS. (h) WCA of O-CHS. The lattice spacings of 0.246 nm shown in Fig.s S1b and S1f are in good agreement with the (111) planes of Cu_2O, revealing that these structures are all composed of Cu_2O material. Additionally, the lattice spacing of 0.212 nm shown in Fig. S1b, corresponds to the (200) plane of Cu_2O.

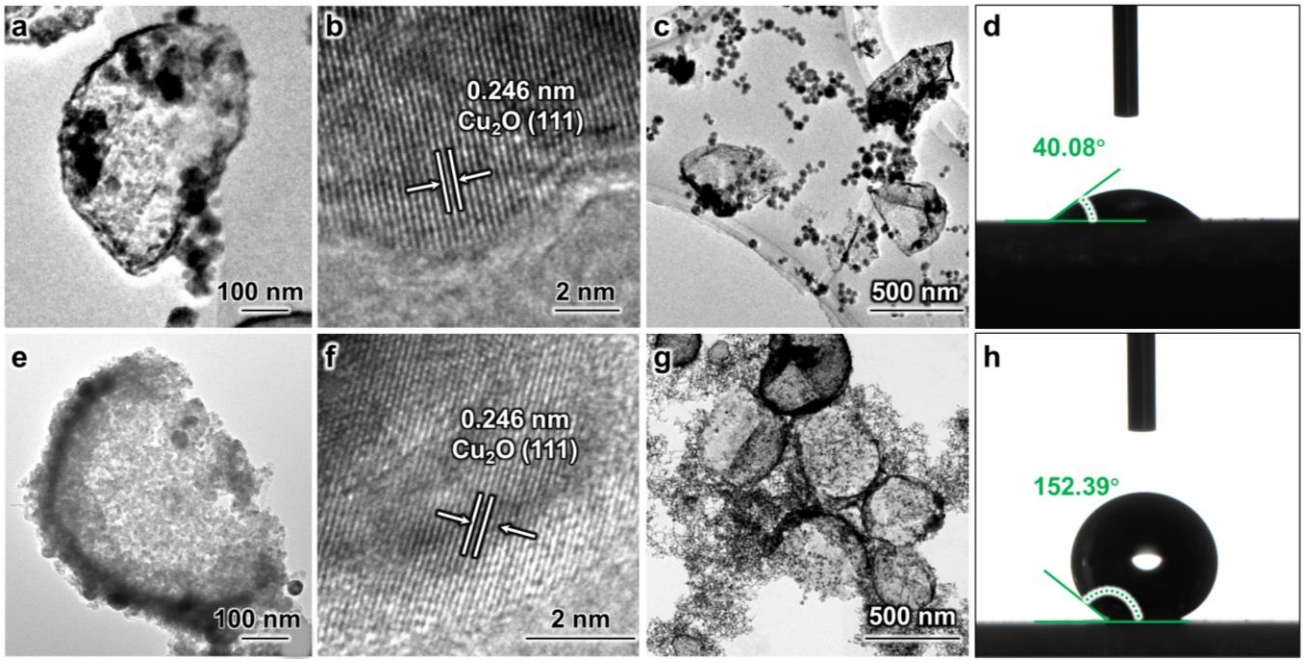

Fig. S2 Morphologies and wettability of CNS and O-CNS. (a, c) TEM images of CNS. (b) HRTEM image of CNS. (d) WCA of CNS. (e, g) TEM images of O-CNS. (f) HRTEM image of O-CNS. (h) WCA of O-CNS. As depicted in Fig.s S2a and S2c, the morphology of CNS differs from that of CHS. While CHS exhibits a completely hollow spherical structure, CNS appears as an irregular hemispherical shape with a broken spherical structure. This indicates that CNS indeed loses the enclosed hollow structure. Upon hydrophobic modification, the images of O-CNS shown in Fig. S2e to S2g resemble the corresponding images of CNS, suggesting that the hydrophobic modification has no impact on the morphology of O-CNS. Furthermore, the lattice spacings of 0.246 nm shown in Fig.s S2b and S2f align well with the (111) planes of Cu_2O, confirming that these structures are composed of Cu_2O material.

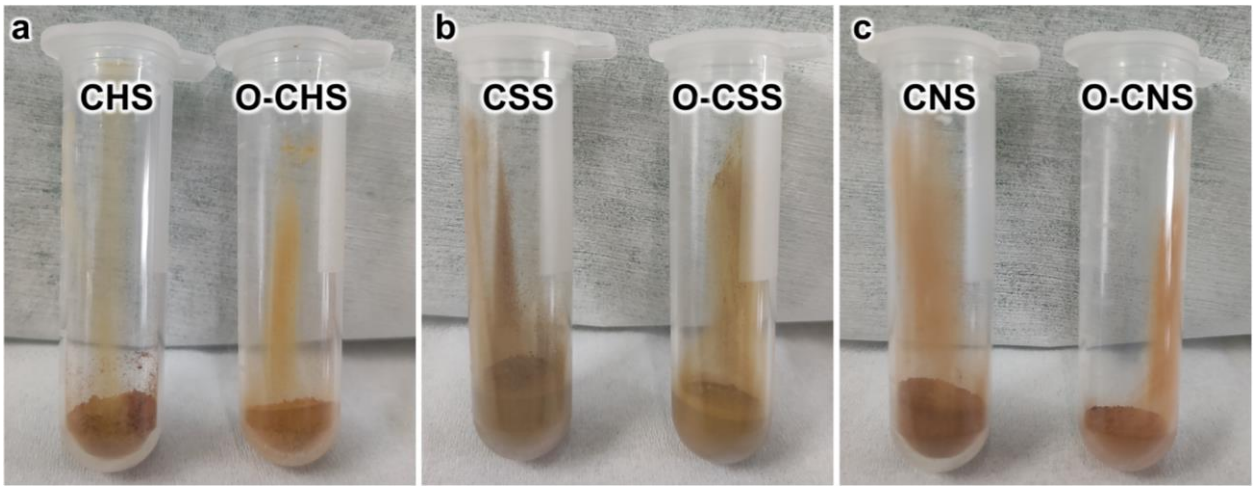

Fig. S3 Photographs of the as-prepared Cu_2O photocatalysts. (a) CHS and O-CHS. (b) CSS and O-CSS. (c) CNS and O-CNS.

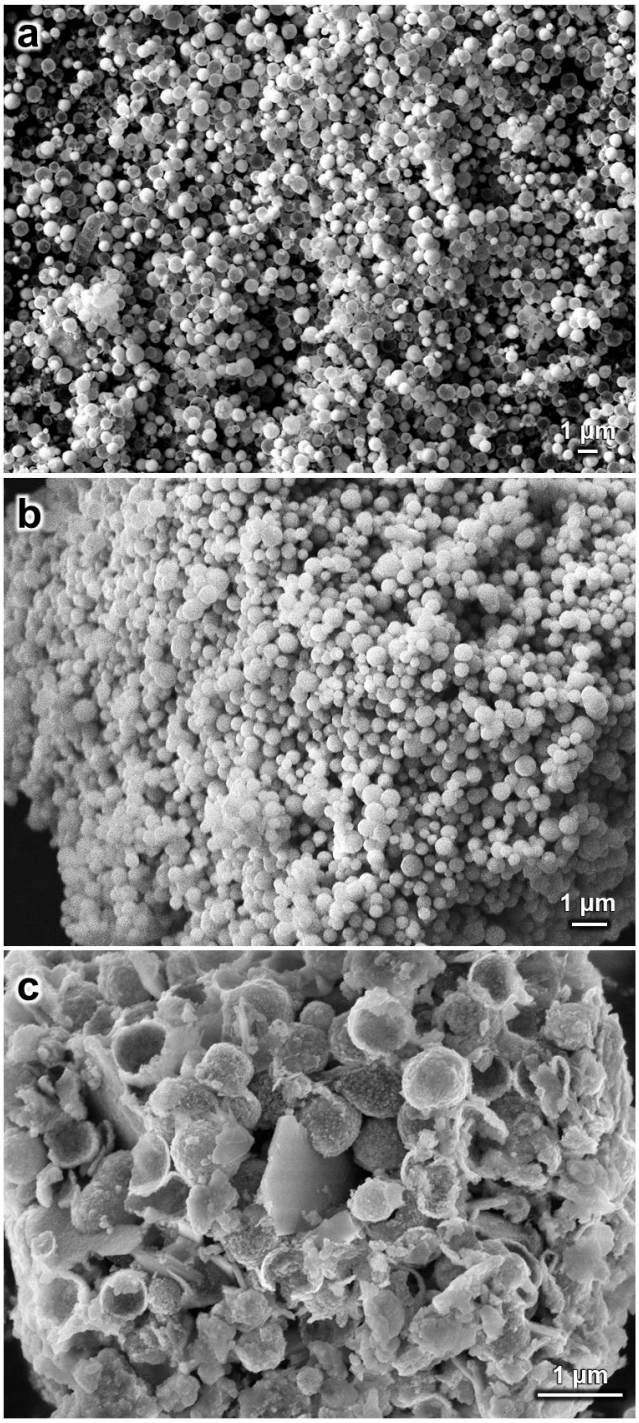

Fig. S4 SEM images. (a to c) SEM images of the obtained O-CHS, O-CSS, and O-CNS, respectively.

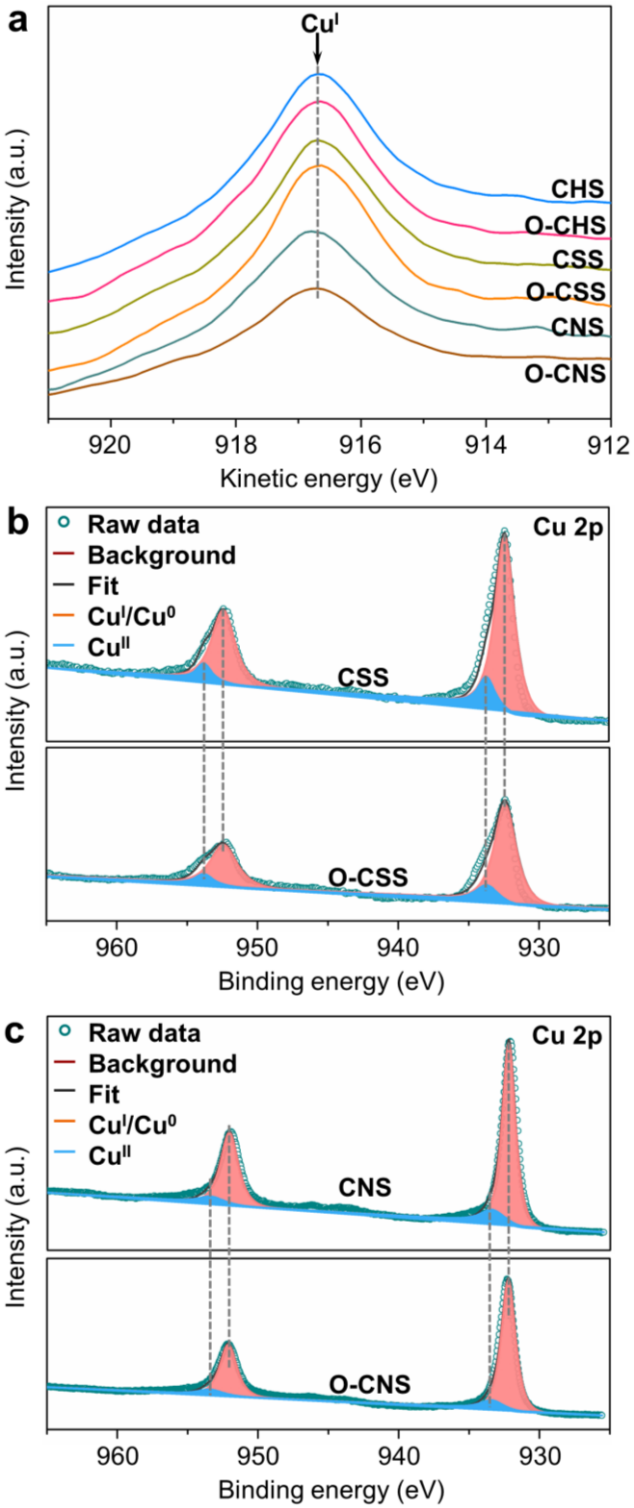

Fig. S5 XPS results of catalysts. (a) Cu LMM Auger spectra of CHS, O-CHS, CSS, O-CSS, CNS, and O-CNS. (b) High-resolution Cu 2p XPS spectra of CSS and O-CSS. (c) High-resolution Cu 2p XPS spectra of CNS and O-CNS.

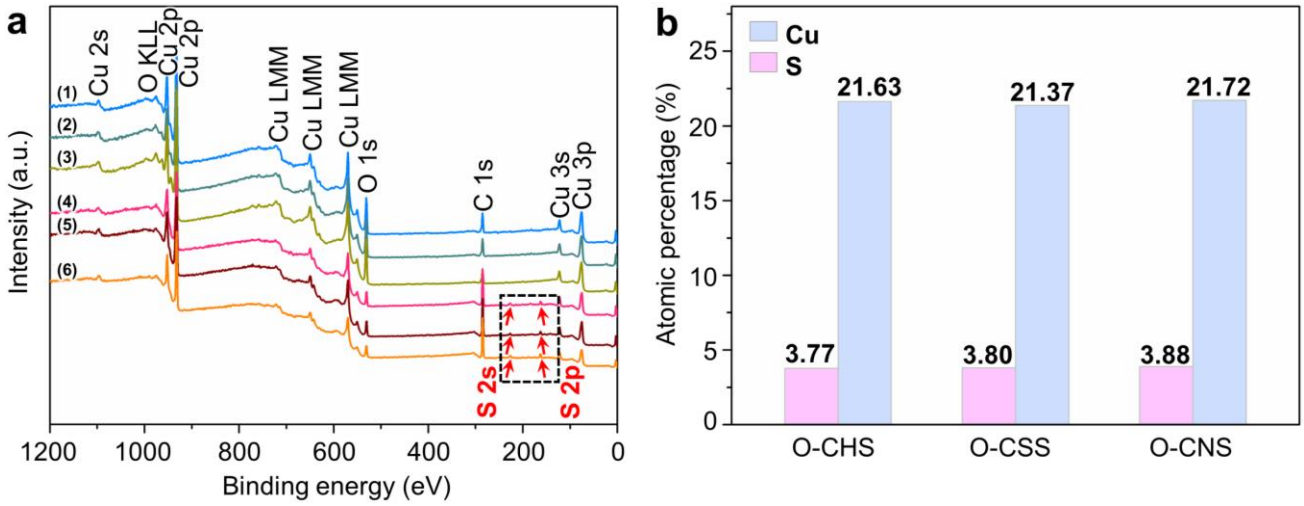

Fig. S6 XPS survey results of catalysts. (a) XPS survey spectra of CHS (1), CSS (2), CNS (3), O-CHS (4), O-CSS (5), and O-CNS (6). (b) The atomic percentages of S and Cu obtained from XPS measurements for O-CHS, O-CSS, and O-CNS. The low atomic percentages of S show low sulfur contents, suggesting a low amount of DDT used for hydrophobic modification. Additionally, the similar atomic percentages of S and Cu for O-CHS, O-CSS, and O-CNS indicate comparable situations regarding the hydrophobic modification.

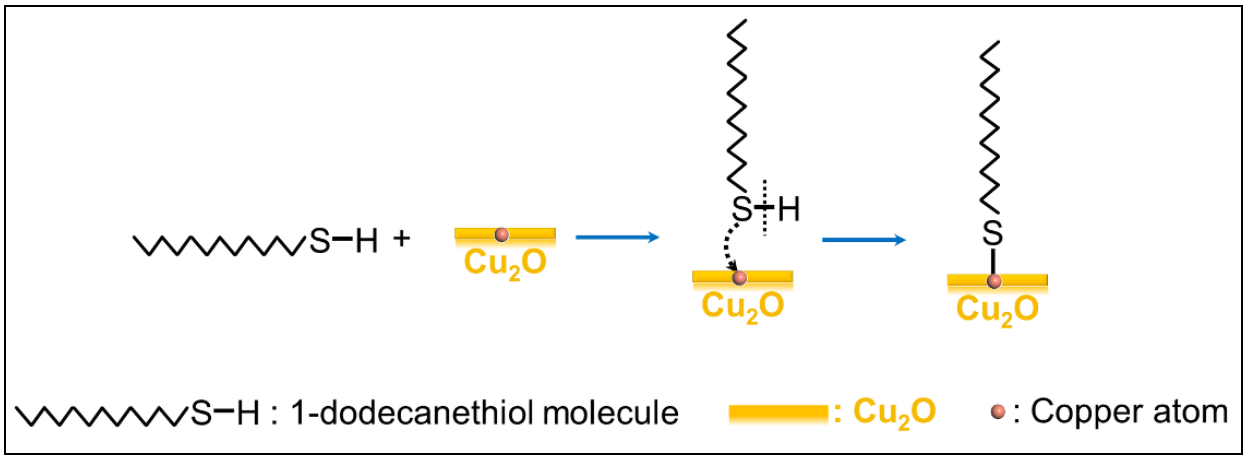

Fig. S7 Interaction between 1-dodecanethiol and Cu_2O. Schematic of 1-dodecanethiol molecule adsorbed on the Cu_2O surface. During the hydrophobic modification process, the -S-H bond in 1-dodecanethiol is broken first, followed by the formation of the S-Cu^I bond to graft 1-dodecanethiol onto the surface of Cu_2O.

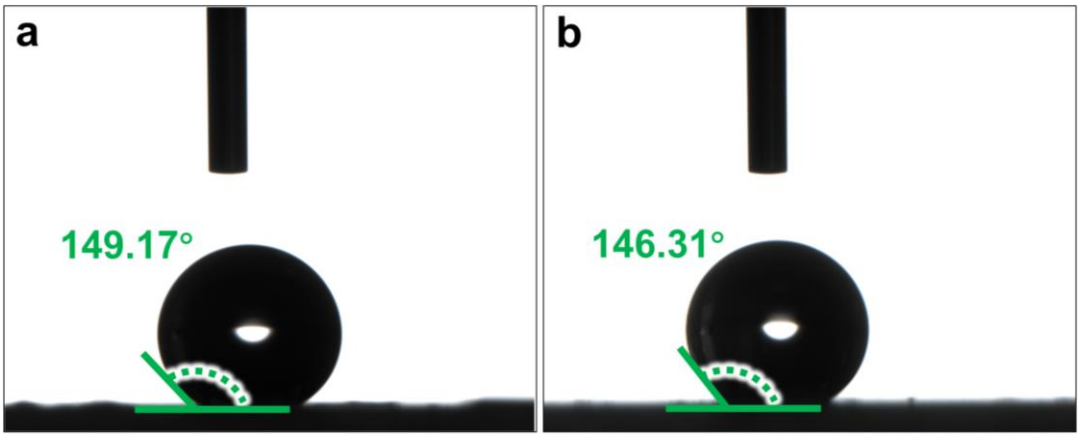

Fig. S8 Water contact angles of O-CHS. (a) After 6 hours of Xe lamp irradiation. (b) After a prolonged storage period of 20 days.

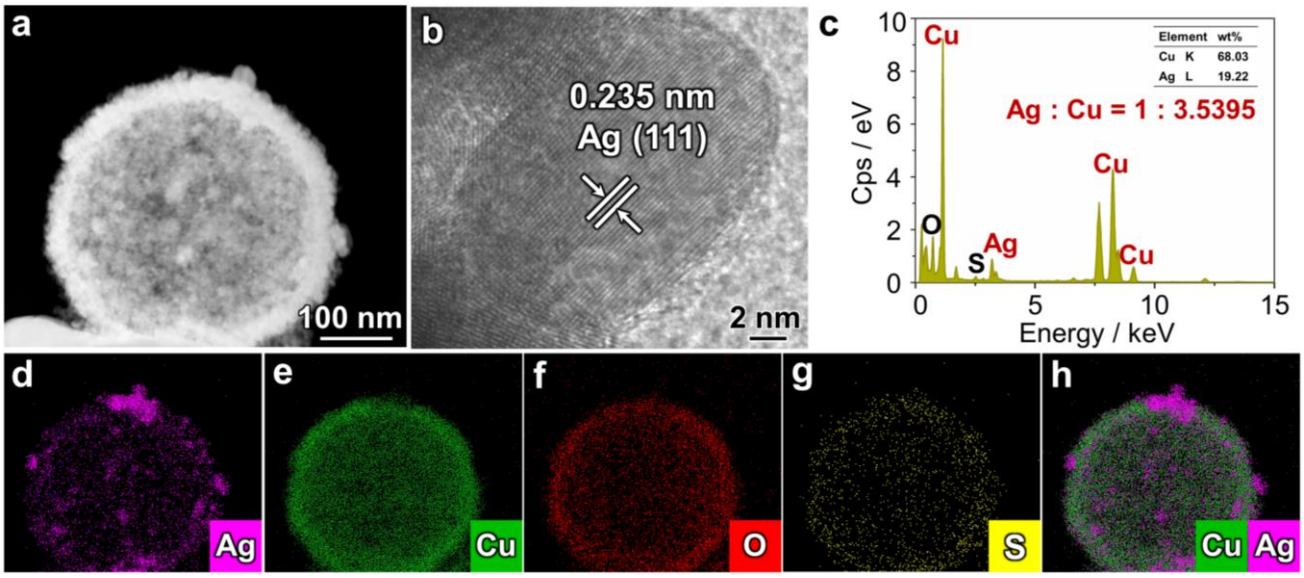

Fig. S9 Ag^+ probe experiment for O-CHS. (a) High-angle annular dark field scanning transmission electron microscopy (HAADF-STEM) image, (b) HRTEM image, and (c) EDS spectrum of O-CHS loaded with Ag particles. (d to g) EDS elemental mapping images for Ag, Cu, O, and S of O-CHS loaded with Ag particles, respectively. (h) Cu and Ag overlap signals of O-CHS loaded with Ag particles. A typical lattice distance of 0.235 nm corresponding to the (111) facet of Ag is clearly discernible in Fig. S9b. Furthermore, the EDS mapping images (Fig. S9d to S9h) display the distribution of Ag particles on the O-CHS surface. More importantly, the Ag/Cu ratio for O-CHS (1:3.5395) shown in Fig. S9c is almost equal to that for CHS (1:3.5378) shown in Fig. S10c. This similarity suggests that the charge transfer process from the surface to the adsorbate remains largely unaffected by the hydrophobic treatment. Because during the Ag^+ probe experiment, Ag^+ is reduced to Ag particles by the electrons migrating to the catalyst surface, while holes are consumed by the sacrificial methanol. Thus, by comparing the quantity of Ag particles obtained, we can infer the extent of carrier migration to the catalyst surface. Therefore, the comparable Ag/Cu ratios in O-CHS and CHS imply a similar charge transfer situation, indicating that the hydrophobic treatment has no obvious effect on the surface-to-adsorbate charge transfer, which would be due to the small amount of 1-dodecanethiol used.

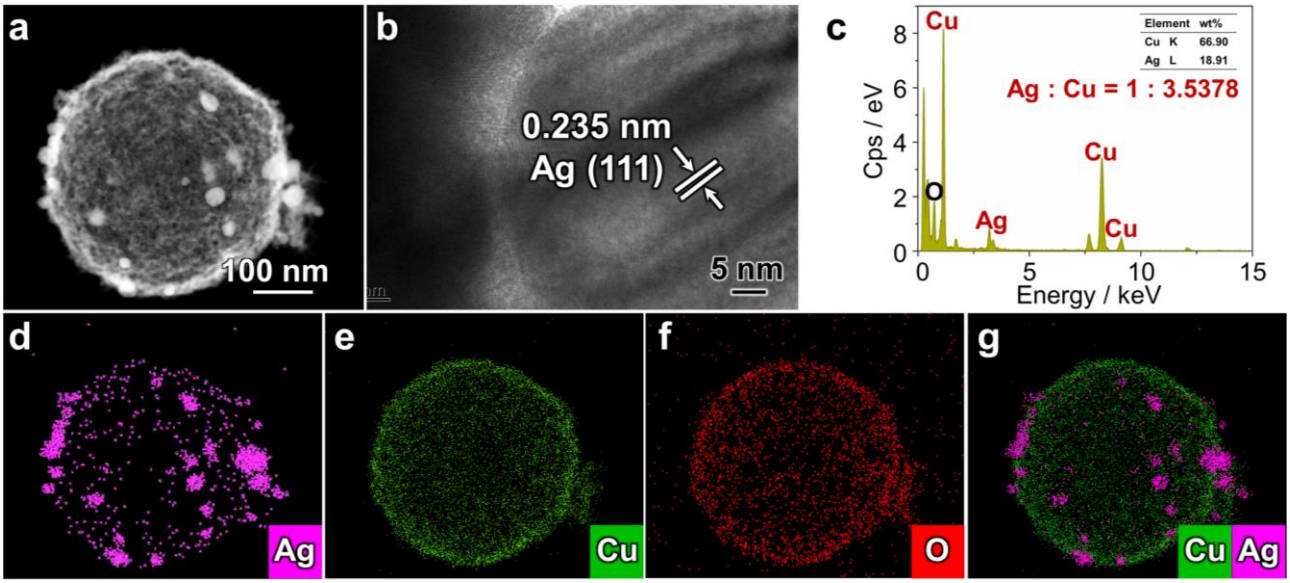

Fig. S10 Ag^+ probe experiment for CHS. (a) HAADF-STEM image, (b) HRTEM image, and (c) EDS spectrum of CHS loaded with Ag particles. (d to f) EDS elemental mapping images for Ag, Cu, and O of CHS loaded with Ag particles, respectively. (g) Cu and Ag overlap signals of CHS loaded with Ag particles. Similar to Fig. S9, a characteristic lattice distance of 0.235 nm corresponding to the (111) facet of Ag is distinctly observed. The EDS mapping images illustrate the distribution of Ag particles on the CHS surface, thereby confirming the successful synthesis of CHS loaded with Ag particles.

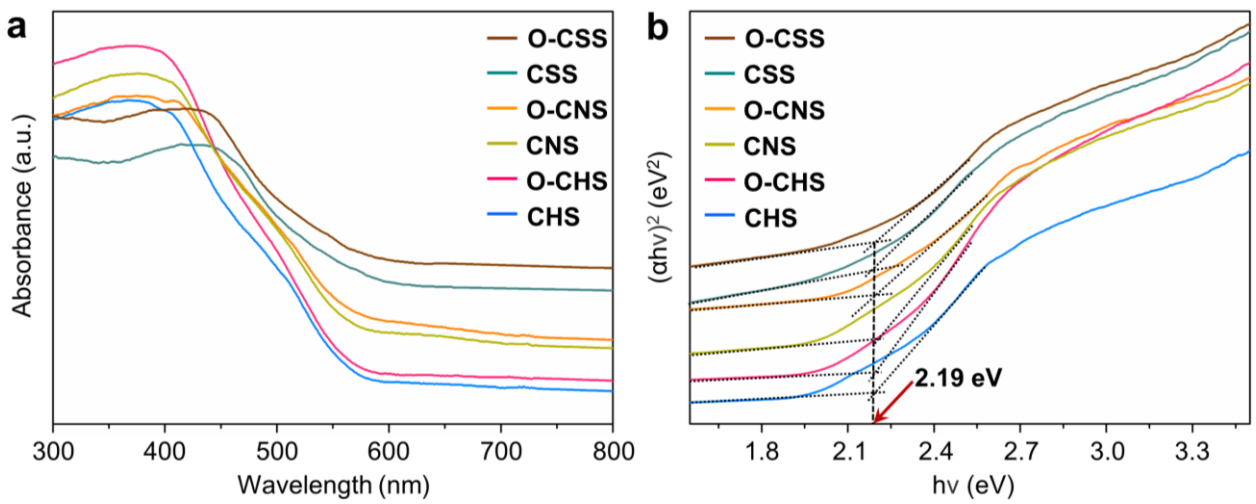

Fig. S11 Light absorption characterizations. (a) UV-vis diffuse reflectance spectra and (b) Tauc plots of CHS, O-CHS, CSS, O-CSS, CNS, and O-CNS.

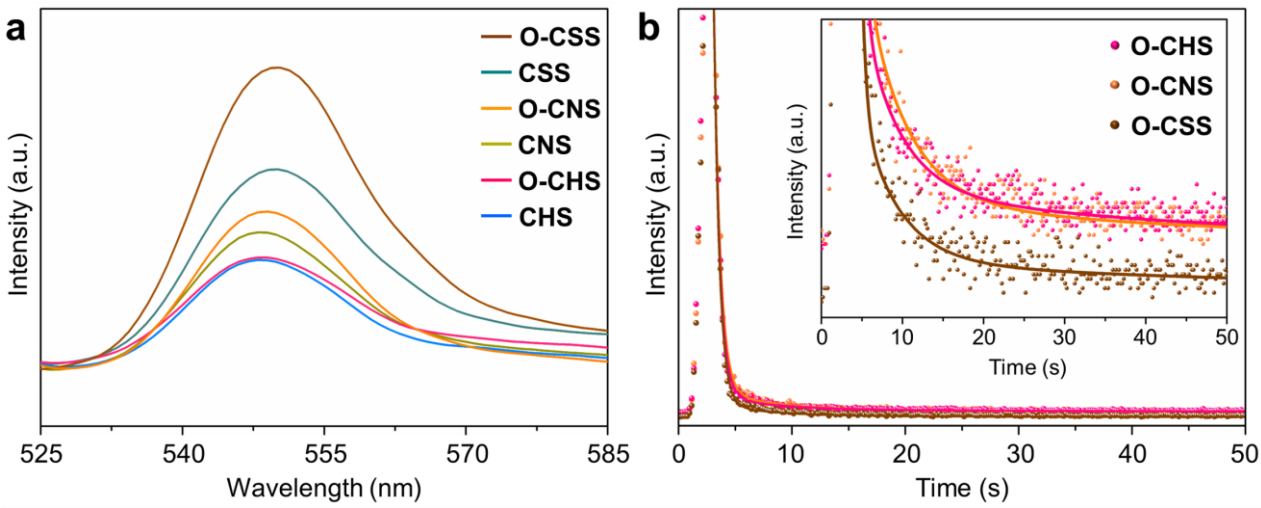

Fig. S12 Photoluminescence (PL) characterizations. (a) Steady-state PL spectra under 350 nm laser irradiation with a 510 nm filter of CHS, O-CHS, CSS, O-CSS, CNS, and O-CNS. (b) Time-resolved PL spectra (TRPL) of O-CHS, O-CNS, and O-CSS under 350 nm laser irradiation. The decay curves were obtained by fitting the observed data (the dots in Fig. S12b) using the following equations: $R(t) = B_1\exp(-t/\tau_1) + B_2\exp(-t/\tau_2) + B_3\exp(-t/\tau_3)$. $\tau_a = (B_1\tau_1^2 + B_2\tau_2^{2+} B_3\tau_3^2)/(B_1\tau_1 + B_2\tau_2 + B_3\tau_3)$. The corresponding fitted parameters are illustrated in Table S2.

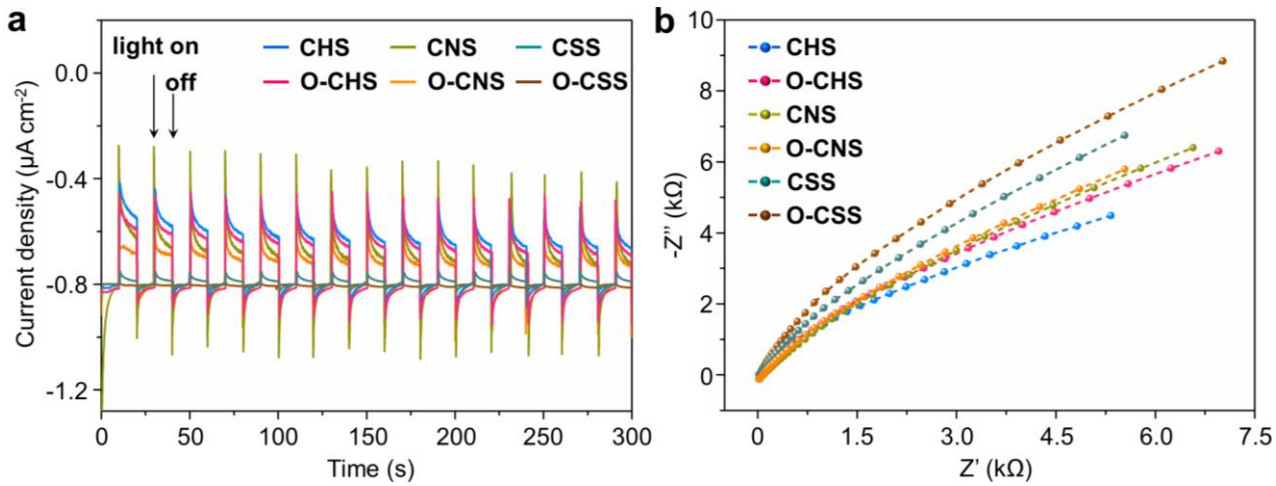

Fig. S13 Photoelectrochemical characterizations. (a) Transient photocurrent curves of CHS, O-CHS, CSS, O-CSS, CNS, and O-CNS with light on/off cycles under visible light irradiation. (b) Electrochemical impedance spectra (EIS) measured in an aqueous solution of Na_2SO_4 (0.02 M) for CHS, O-CHS, CSS, O-CSS, CNS, and O-CNS.

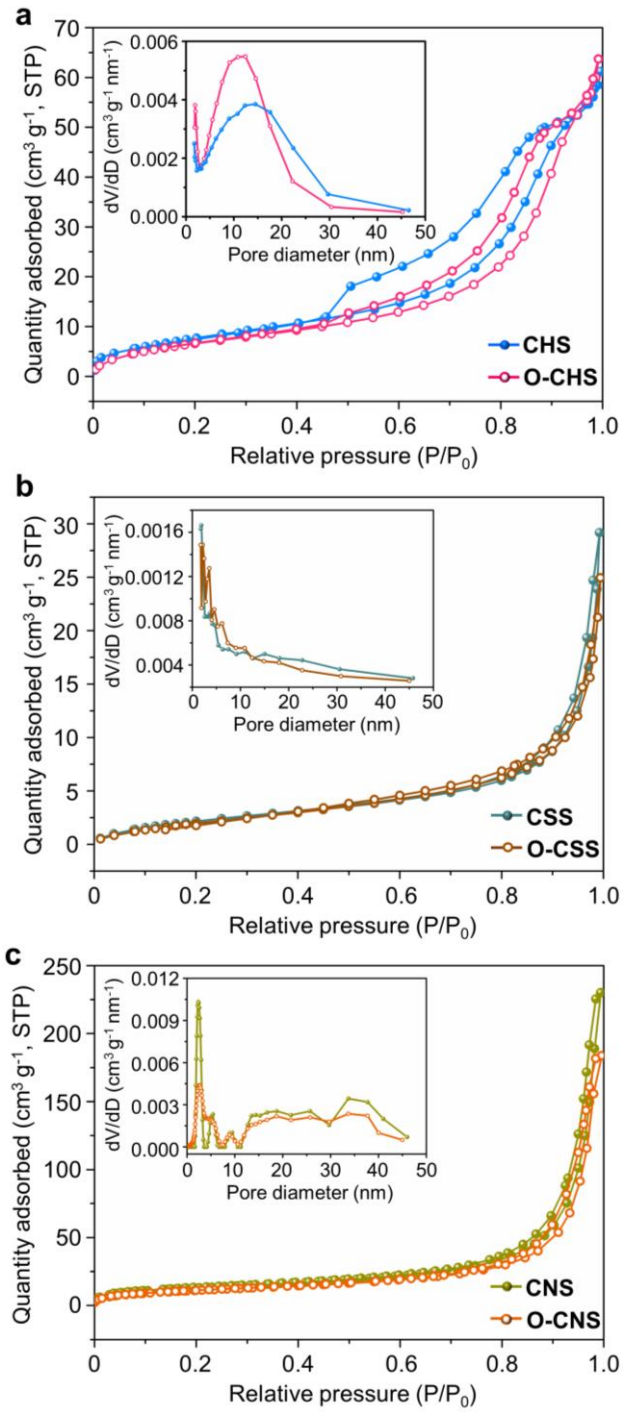

Fig. S14 N_2 adsorption-desorption measurements. N_2 adsorption-desorption isotherms and pore diameter distributions of (a) CHS and O-CHS, (b) CSS and O-CSS, and (c) CNS and O-CNS. As depicted in Table S2, the BET surface areas of CHS, O-CHS, CNS, and O-CNS are larger than those of CSS and O-CSS, thereby providing more active sites for reactions. This finding can be closely related to the structural advantages associated with the hollow structure and nanosheet morphology. Additionally, when compared to the unmodified CHS, CNS, and CSS, the corresponding modified O-CHS, O-CNS, and O-CSS exhibit slightly decreased BET surface areas and average pore diameters, illustrating the modest impact of hydrophobic modification.

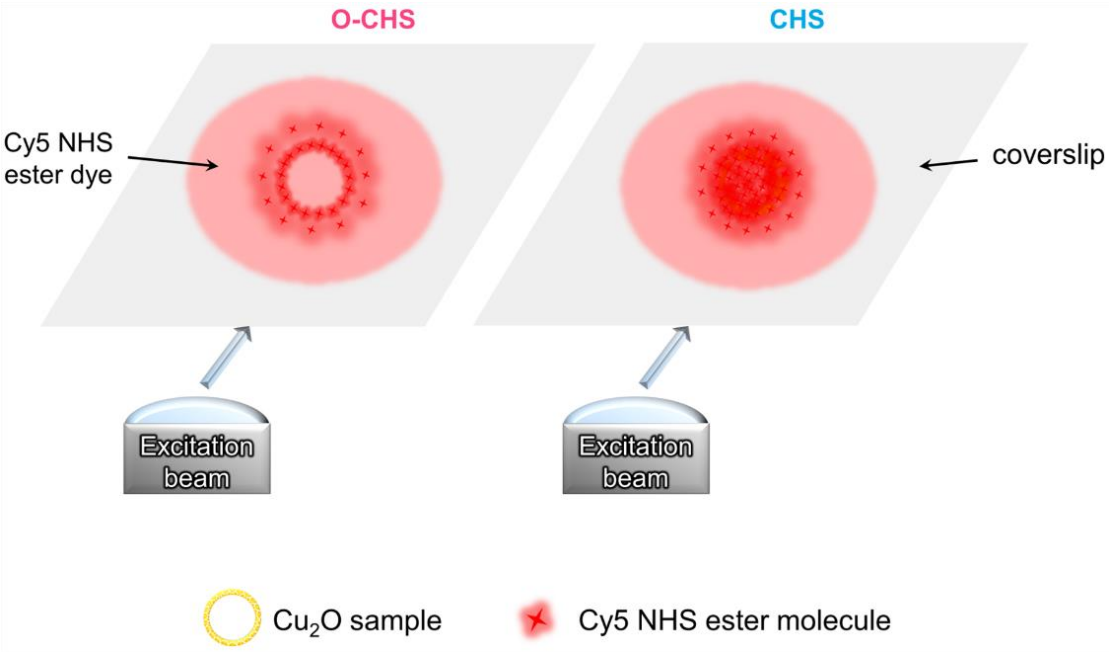

Fig. S15 Schematic of total internal reflection fluorescence microscope (TIRFM) measurements. The fluorescence performance of O-CHS (left) and CHS (right) after dyeing with Cy5 NHS ester under 635 nm excitation in TIRFM measurements is illustrated in Fig. S15. Theoretically, fluorescent molecules dissolved in water can penetrate into the cavity of CHS through the mesopores. Thus, fluorescence signals would be observed both in the interior and exterior of CHS. Conversely, in the case of O-CHS, the superhydrophobic surface poses a challenge for fluorescent molecules to penetrate the shell and access the cavity. Instead, they tend to accumulate in significant quantities around the shell, leading to high fluorescence intensity in those regions. Additionally, the fluorescent signal near the Cu_2O sample consistently exhibits greater intensity compared to the bulk environment, which may be attributed to the adsorption effect of solid Cu_2O samples on the dyes.[11, 12]

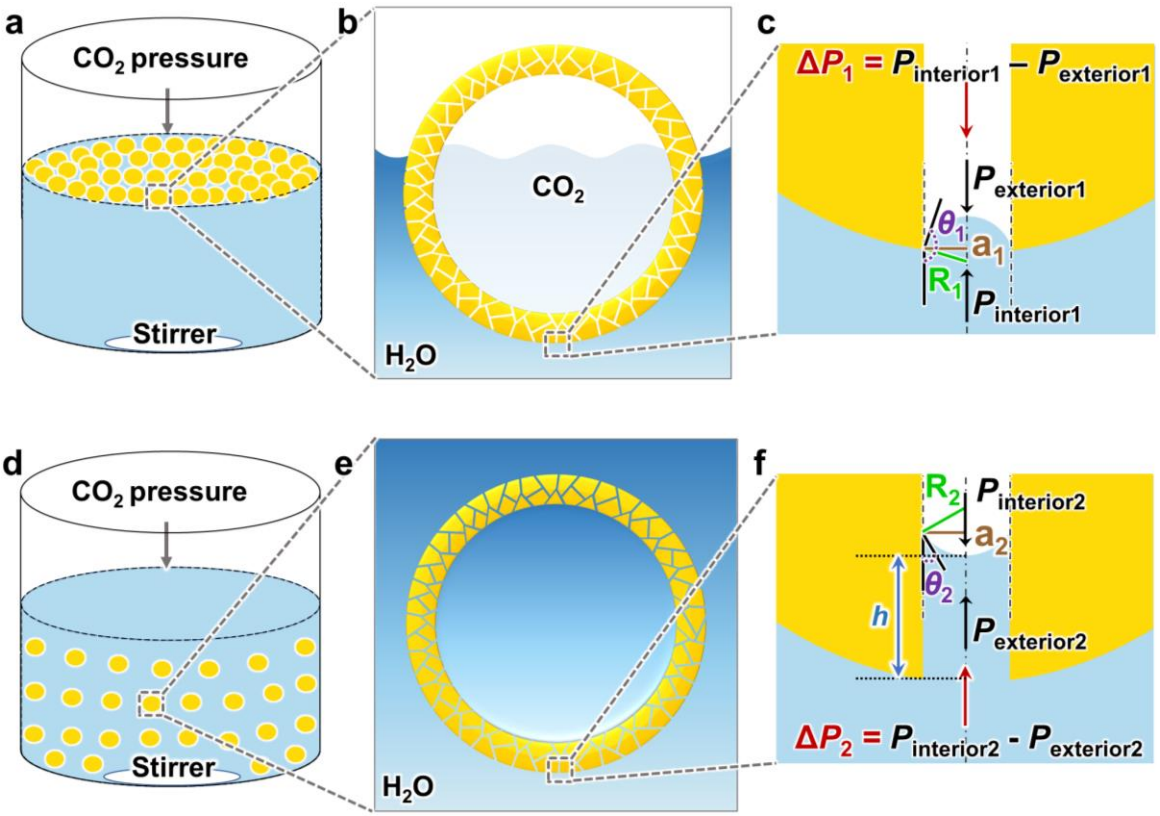

Fig. S16 Schematics for the calculation of the infiltration pressure. (a, d) Schematics of O-CHS and CHS in the reactor, respectively. (b, e) Single particle magnified schematics of O-CHS and CHS in the aqueous solution, respectively. (c, f) Schematics of the liquid-gas interface advancing inside the pore in O-CHS and CHS, respectively. O-CHS is floating on the aqueous solution and CHS is suspended in the aqueous solution. ΔP_1 and ΔP_2 can be calculated according to the detailed description in **Experimental Procedures. Calculation of the infiltration pressure required for water to penetrate the pores**. To maintain hydrostatic equilibrium within CHS, the induced capillary pressure (ΔP_2) will be balanced by the height (h) of the liquid column rising in the pore. This can be calculated using the equation $P_{total} = \Delta P_2 + P_{CO2} = \rho g h$, where ρ represents the density of the liquid and g is the gravitational acceleration. Even in the limiting state where the pressure of CO_2 above the liquid surface (P_{CO2}) is zero, the liquid column height (h) still needs to reach ~440 m to balance ΔP_2. This value of h is much greater than the depth of pores in the CHS shell. Consequently, water can pass through the pores entirely and enter the interior of the hollow space.

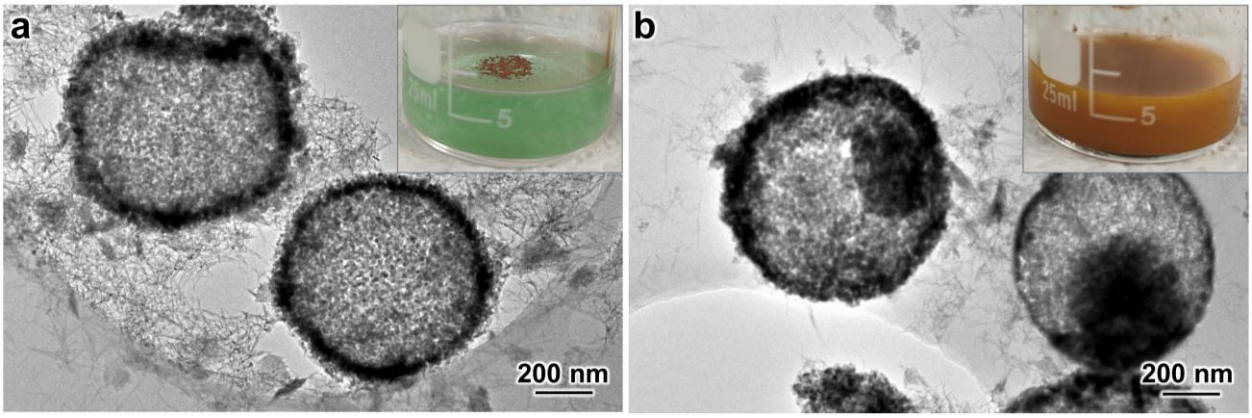

Fig. S17 $Cu(OH)_2$ probe experiments. (a, b) TEM images for O-CHS and CHS after $Cu(OH)_2$ probe experiment, respectively. Corresponding insets in Fig.s S17a and S17b are the photographs containing O-CHS and CHS after the addition of NaOH solution, respectively. As shown in the inset, the formed $Cu(OH)_2$ precipitate is visibly separated from O-CHS. Conversely, in the case of CHS, the $Cu(OH)_2$ precipitate forms a homogeneous whole with CHS.

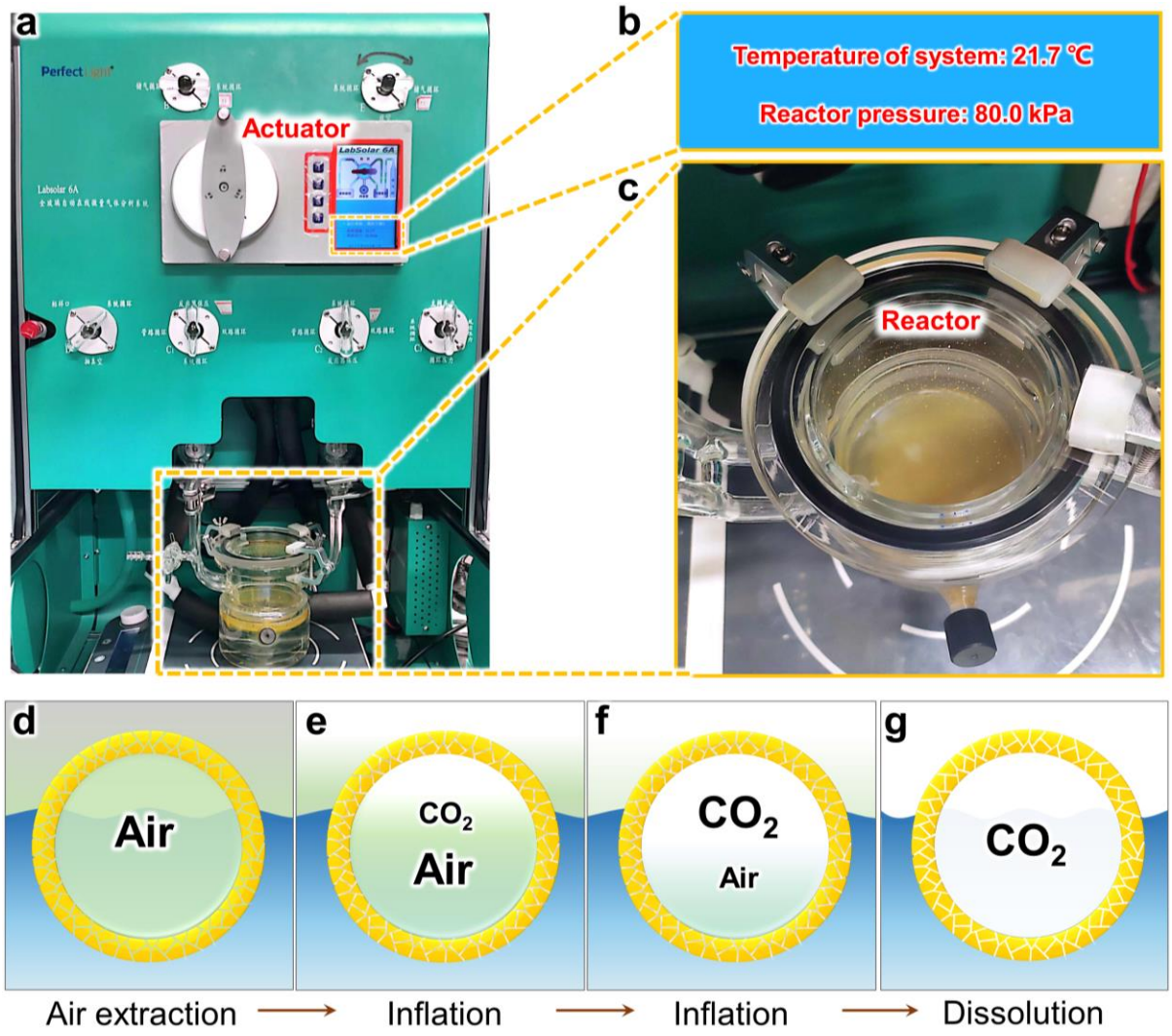

Fig. S18 Pre-treatment process before the CO_2 photoreduction test. (a) Device used. (b) Enlarged view of the temperature and pressure displayed on the Labsolar 6A actuator. The actuator can display the real-time CO_2 pressure in the gas phase of the system and the temperature of the connected Labsolar 6A. (c) Reactor used in the tests. It can be seen that the superhydrophobic catalyst is floating on the aqueous solution. (d to g) Schematics of the variations in gas composition within the hollow space of O-CHS during the extraction-inflation and CO_2 dissolution processes. The color scheme employed in the schematic representation is as follows: water is depicted in blue, O-CHS in yellow, vacuum in gray, residual air in green, and inflated CO_2 in white. Gradient colors are utilized to illustrate the blending of corresponding states. Prior to commencing the overall PCRR, it is necessary to repeatedly evacuate and inflate the reaction system to minimize the presence of air as much as possible. O-CHS floats on the aqueous solution, gaseous CO_2 above the liquid surface will enter the hollow space through the mesopores it contacts during the inflation process. Consequently, CO_2 gradually displaces the residual air present within the hollow space of O-CHS. After the final inflation to 80 kPa, CO_2 will gradually reach the dissolution equilibrium, and the hollow space of O-CHS will be filled with CO_2.

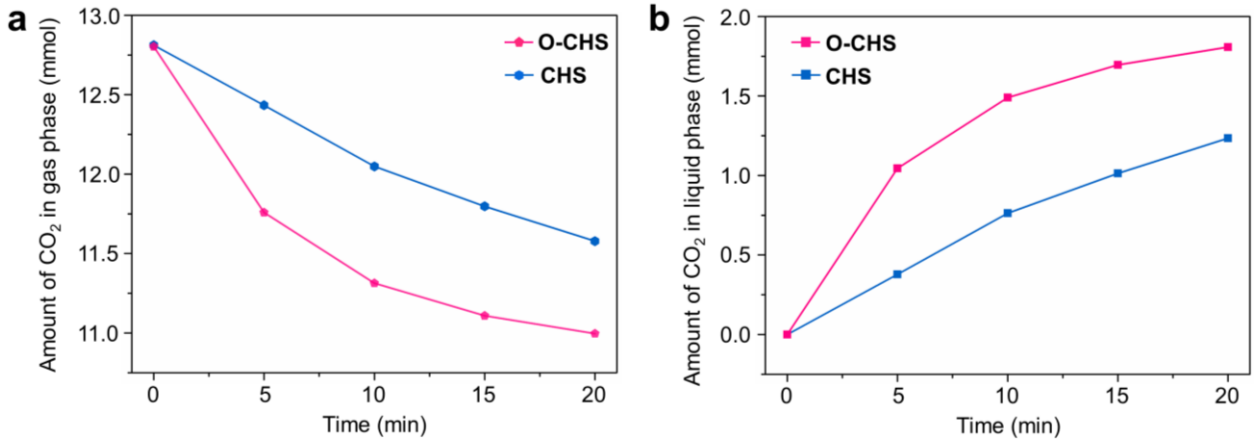

Fig. S19 CO_2 dissolution rate. (a) Changes of relative amounts of CO_2 in the gas phase in the CO_2 photoreduction test system with the dissolution time over O-CHS and CHS. (b) Changes of relative amounts of CO_2 in the liquid phase in the CO_2 photoreduction test system with the dissolution time over O-CHS and CHS.

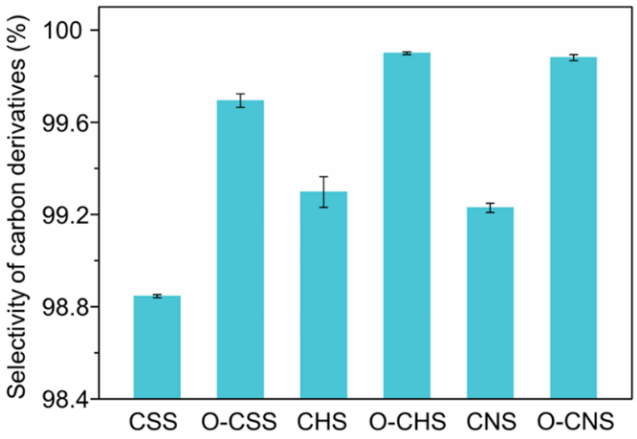

Fig. S20 Selectivity of carbon derivatives. Selectivities of the sum of methanol and ethanol generated over CSS, O-CSS, CHS, O-CHS, CNS, and O-CNS.

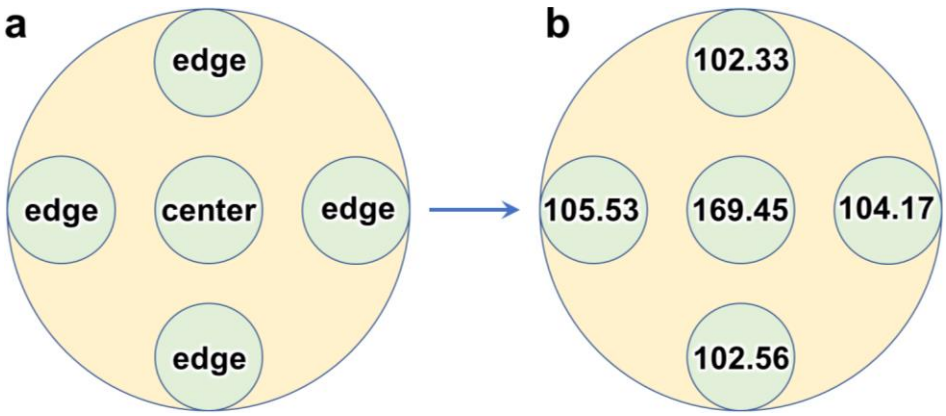

Fig. S21 Light intensity test. (a) Five different test positions. (b) Corresponding test values.

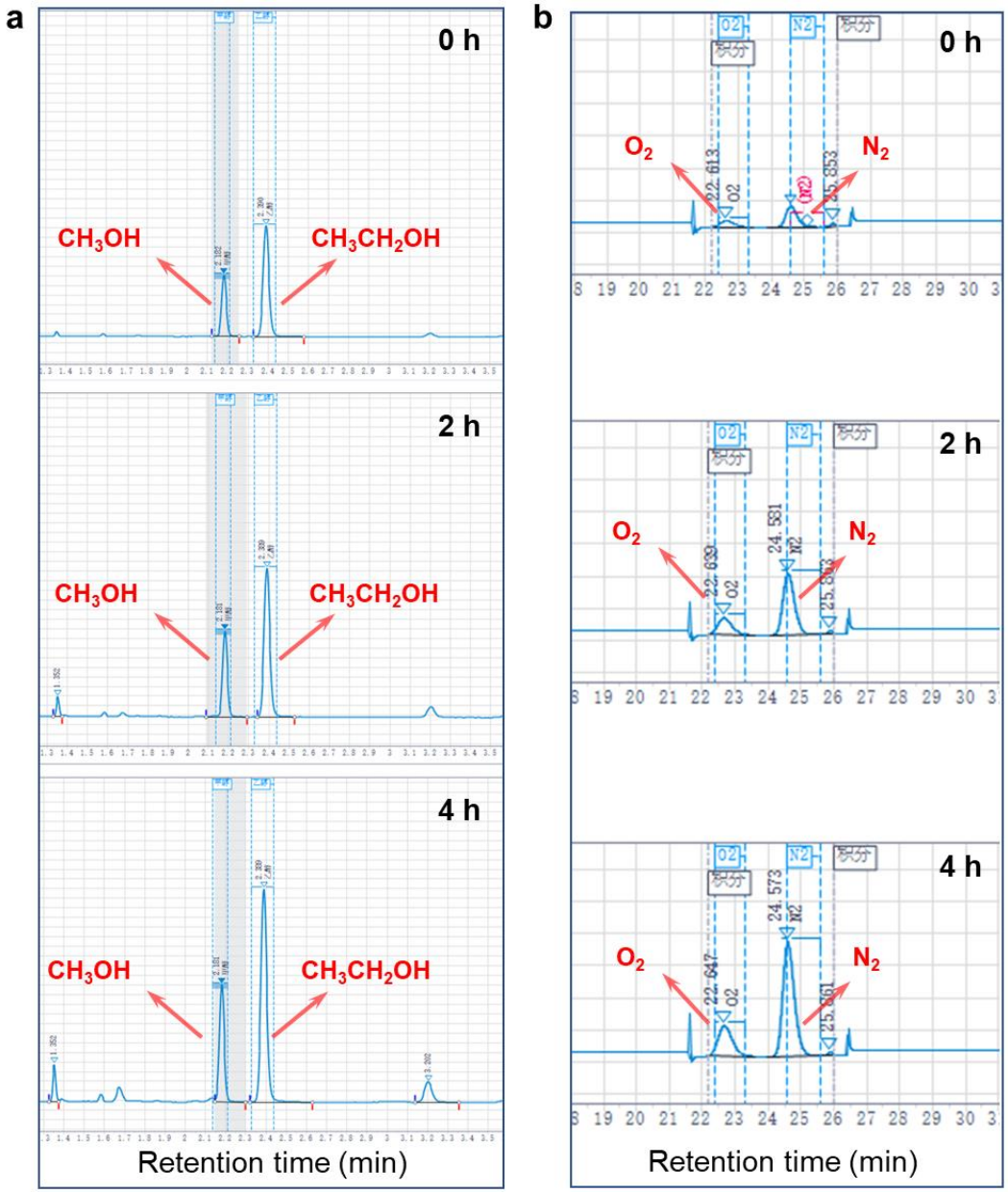

Fig. S22 Original data obtained from gas chromatography (GC). (a, b) Original data of methanol and ethanol, and O_2 generation over O-CHS detected by GC, respectively. The intensity of characteristic peaks corresponding to methanol, ethanol, and O_2 exhibits a clear increase as the reaction time progressed.

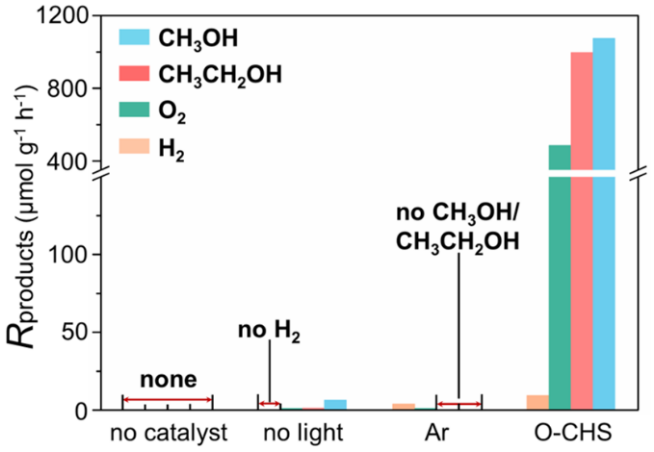

Fig. S23 Control experiments. Several control experiments were conducted to ensure that obtained products originated from the overall PCRR. Firstly, a test was performed using CO_2 and H_2O as reactants, but without the presence of a photocatalyst. In this case, no carbon derivatives were detected, indicating that the overall PCRR could not occur in the absence of the photocatalyst. When the test was performed with the catalyst and CO_2, but without Xe lamp irradiation, only very small amounts of carbon derivatives were obtained, which may result from natural light-induced PCRR. Additionally, when the reactor was vacuumed and purged Ar instead of CO_2, no carbon derivatives were detected under light irradiation in the presence of water and the catalyst, demonstrating that the carbon source for ethanol and methanol production in the overall PCRR was CO_2.

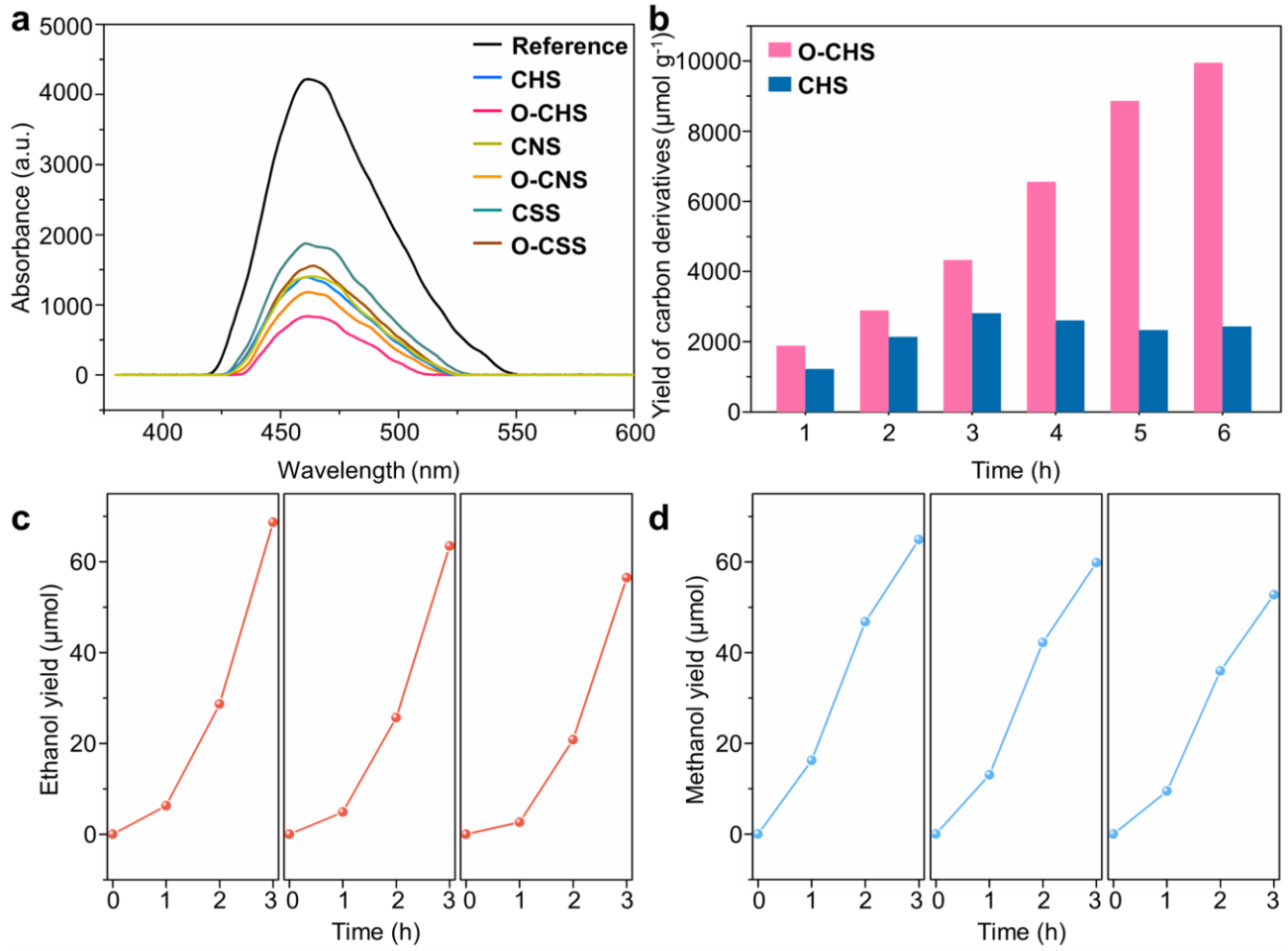

Fig. S24 Supplemental overall PCRR performance. (a) PL spectra of the scopoletin assay of the reaction solution after the overall PCRR using different catalysts. As the amount of H_2O_2 in the reaction solution was low, a sensitive chemiluminescence detection method by scopoletin assay was performed. The fluorescent scopoletin could be oxidized by H_2O_2 in the presence of horseradish peroxidase, leading to the loss of its fluorescence. Thus, a higher intensity of the emission peak for scopoletin at 463 nm in the PL spectra indicates a lower concentration of H_2O_2 in the reaction solution, and vice versa. By comparing the results obtained from the reference (experiment without reaction solution) and various photocatalysts, it can be inferred that a small amount of H_2O_2 is generated over each photocatalyst. (b) Yields of carbon derivatives on O-CHS and CHS as a function of irradiation time. (c) Activity recycle tests of photocatalytic CO_2 to ethanol for O-CHS. (d) Activity recycle test of photocatalytic CO_2 to methanol for O-CHS.

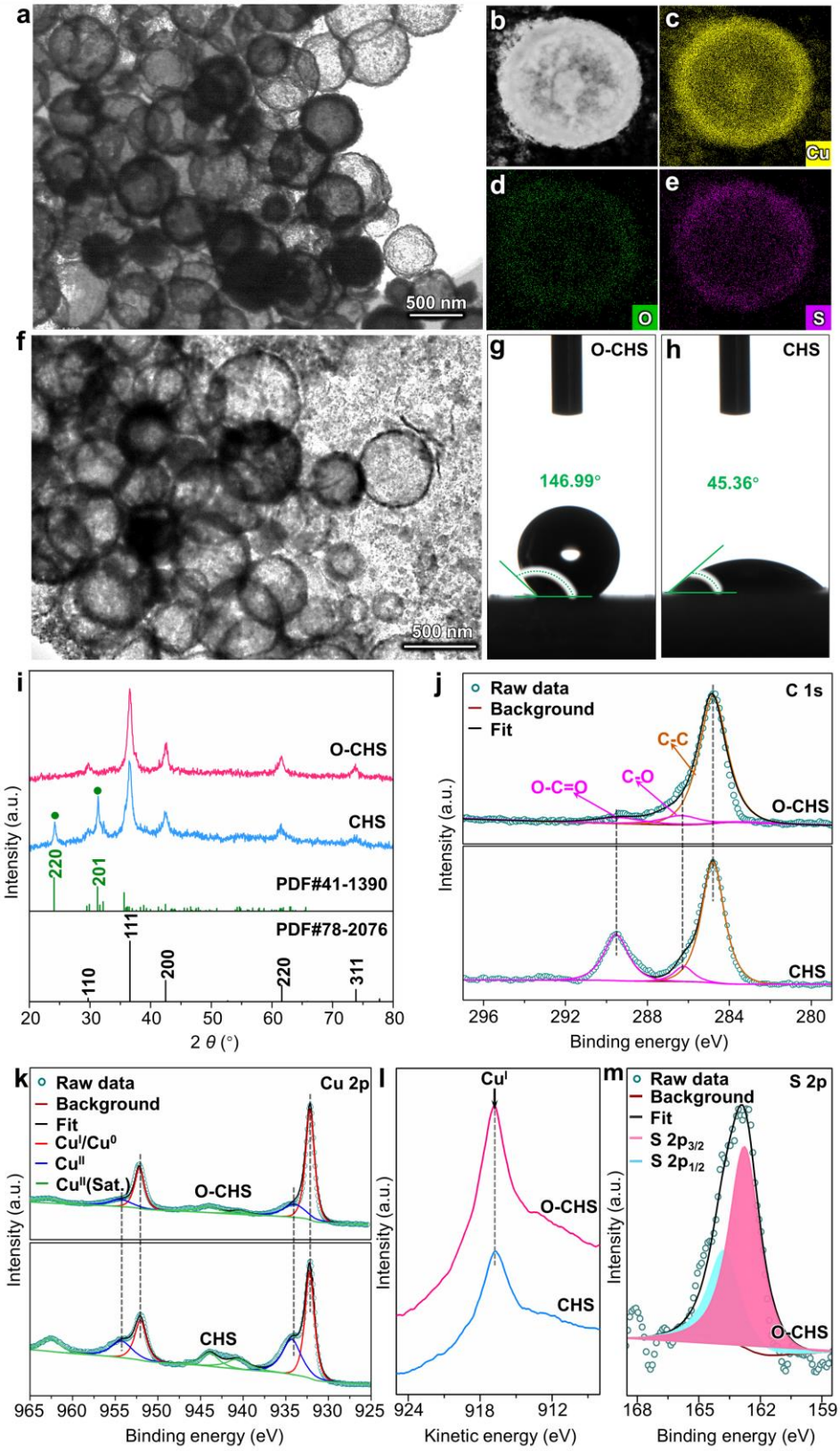

Fig. S25 Characterizations of O-CHS and CHS after reaction. (a) TEM image of O-CHS. (b) HAADF-STEM image of O-CHS. (c - e) EDS mapping images of Cu, O, and S for O-CHS, respectively. (f) TEM image of CHS. (g, h) WCAs of O-CHS and CHS, respectively. (i) XRD patterns, (j) C 1s XPS spectra, (k) Cu 2p XPS spectra, and (l) Cu LMM Auger spectra of O-CHS and CHS. (m) High-resolution S 2p XPS spectra of O-CHS. The TEM image of the spent O-CHS illustrates that there is no significant change in the hollow structure after 6 h of reaction (Fig. S25a). The HAADF-ATEM image of O-CHS also shows the obvious hollow sphere structure for O-CHS after reaction (Fig. S25b). EDS mapping images reveal that S is still evenly distributed on the surface of O-CHS, indicating the stable interaction between DDT and Cu_2O on the surface of O-CHS (Fig. S25c-S25e). However, the TEM

image of spent CHS displays that there are many fragmentations after 6 h of reaction, indicating the collapse of the hollow structure for CHS (Fig. S25f). The WCAs of spent O-CHS and CHS are measured to be 146.99° and 45.36°, respectively, which are similar to the corresponding WCAs of O-CHS and CHS before reaction (Figs. S25g and S25h). This further suggests the hydrophobic stability of O-CHS during the overall PCRR. Additionally, XRD and XPS measurements are adopted to detect the structural changes of O-CHS and CHS after reaction. It can be seen that there is no change in the XRD pattern of the spent O-CHS (Fig. S25i). However, the XRD pattern of the spent CHS exhibits additional characteristic diffraction peaks at 24.10° and 31.24°, which are assigned to the (220) and (201) planes of basic copper carbonate ($Cu_2(OH)_2CO_3$), respectively (JCPDS Card No. 41-1390)[13]. The presence of $Cu_2(OH)_2CO_3$ in the spent CHS is further confirmed by the C 1s XPS spectra (Fig. S25j). The sharp peak at 284.8 eV can be attributed to carbon-containing contamination used for spectral calibration. The peaks at 286.2 and 289.5 eV correspond to O-C=O and C-O, respectively, demonstrating the formation of $Cu_2(OH)_2CO_3$.[14] This transformation could be owing to the reoxidation of reduced copper species generated during the overall PCRR, which can occur easily when exposed to air.[15, 16] The greater $Cu_2(OH)_2CO_3$ signal observed for CHS indicates the more reduced copper species formed. Additionally, the main compositions of the spent O-CHS and CHS can still be identified as Cu_2O, as observed by combing the Cu 2p XPS spectra and the Cu LMM Auger spectra (Figs. S25k and S25l). However, the presence of high-intensity shake-up satellites at approximately 940.5, 943.9, and 962.7 eV in Cu 2p XPS spectra, assigned to CuO in CHS, also imply the more severe occurrence of photocorrosion in CHS.[17] In contrast, O-CHS shows better stability. This could be attributed to the protective barrier provided by its superhydrophobic surface, effectively repelling H_2O from the surface of O-CHS. Thus, the electron-mediated photocorrosion involving H_2O of Cu_2O could be weakened.[18, 19] Moreover, due to the faster reaction rate of O-CHS to consume more photogenerated holes, hole-mediated photocorrosion could also be inhibited.[20, 21] Additionally, in order to further verify the stability of DDT absorbed on the surface of O-CHS, S 2p XPS test for O-CHS after reaction was conducted to detect the change in the surface chemical states of S. It can be seen that the binding energies for the S $2p_{3/2}$ core level on O-CHS still exhibit a strong peak at 162.45 eV, falling well within the expected range for a surface thiolate species (RS-Cu). Thus, DDT is still chemically adsorbed on the surface of O-CHS, providing hydrophobicity for O-CHS.

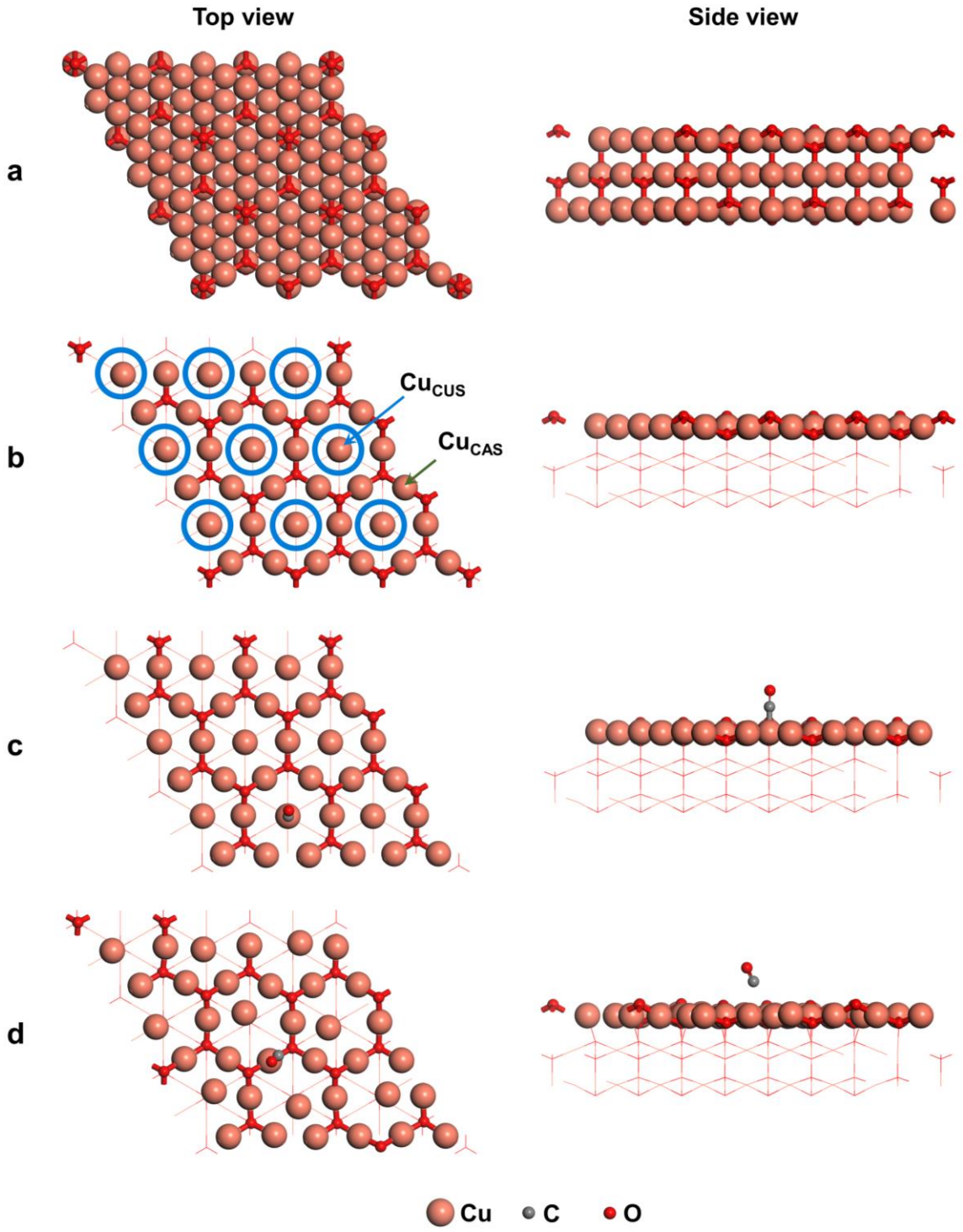

Fig. S26 Top and side views of different configurations. (a) Slab model of the ideal Cu_2O (111) surface. (b) Two different adsorption sites of Cu on Cu_2O (111) surface. (c) Slab model with CO adsorbed on the site of Cu_{CUS}. (d) Slab model with CO adsorbed on the site of Cu_{CAS}. The brown, gray, and red balls represent Cu, C, and O atoms, respectively. The Cu_2O (111) surface is depicted as a periodic (3×3) slab, consisting of three layers (Fig. S26a). To clearly illustrate the different coordination situations of Cu atoms, the ball-stick model is used for the first layer, while the remaining two layers are represented by line segments. As shown in Fig. S26b, Cu_{CUS} represents the coordinatively unsaturated surface Cu atom marked with blue circles, and the other Cu atoms are coordinatively saturated Cu atoms (Cu_{CAS}). CO can form a stable bond with Cu_{CUS} (Fig. S26c), whereas this is not the case for Cu_{CAS} (Fig. S26d). Thus, Cu_{CUS} is selected as the active site for the DFT calculation and there are a total of nine Cu_{CUS} sites on the Cu_2O (111) slab (marked with blue circles in Fig. S26b).

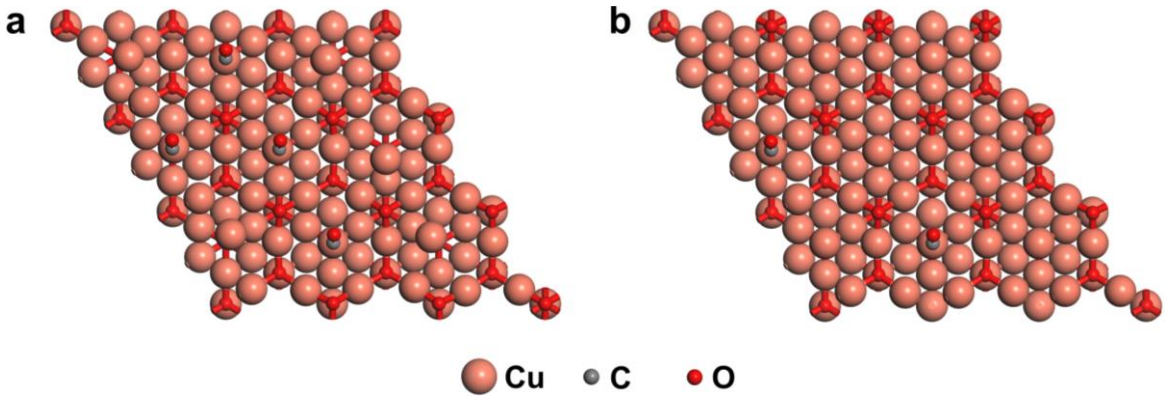

Fig. S27 Configurations at different *CO coverages. (a) High *CO coverage of Cu_2O. (b) Low *CO coverage of Cu_2O. The brown, gray, and red balls represent Cu, C, and O atoms, respectively. Four CO molecules are placed on Cu_{CUS} sites of the Cu_2O model to simulate the high *CO coverage of O-CHS. In contrast, a low *CO coverage of CHS with only two CO molecules placed on Cu_{CUS} sites is adopted. The Gibbs free energy changes (ΔG) for CO adsorption on Cu_{CUS} at different *CO coverages are then calculated. The results of -2.450 and -2.398 eV for high and low *CO coverages, respectively, illustrate the stable binding of CO with Cu_{CUS} (Table S3).

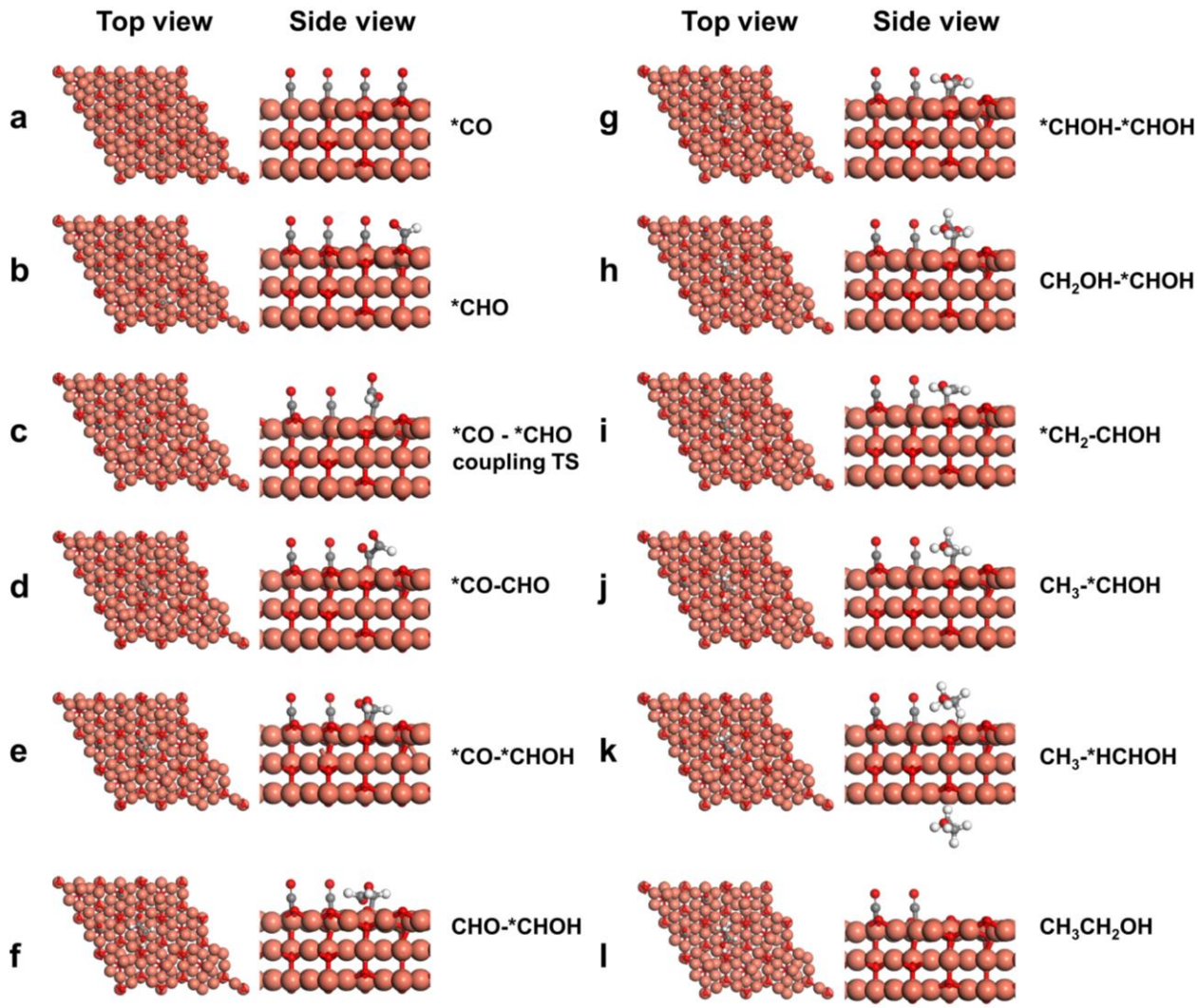

Fig. S28 Top and side views of different configurations for CO_2-to-CH_3CH_2OH conversion at high *CO coverage. (a to l) Top and side views of optimized adsorption configurations for main reaction intermediates during the overall PCRR to ethanol on Cu_2O (111) surface at high *CO coverage. The brown, gray, red, and white balls represent Cu, C, O, and H atoms, respectively. TS means transition state of C-C coupling. * represents surface adsorption.

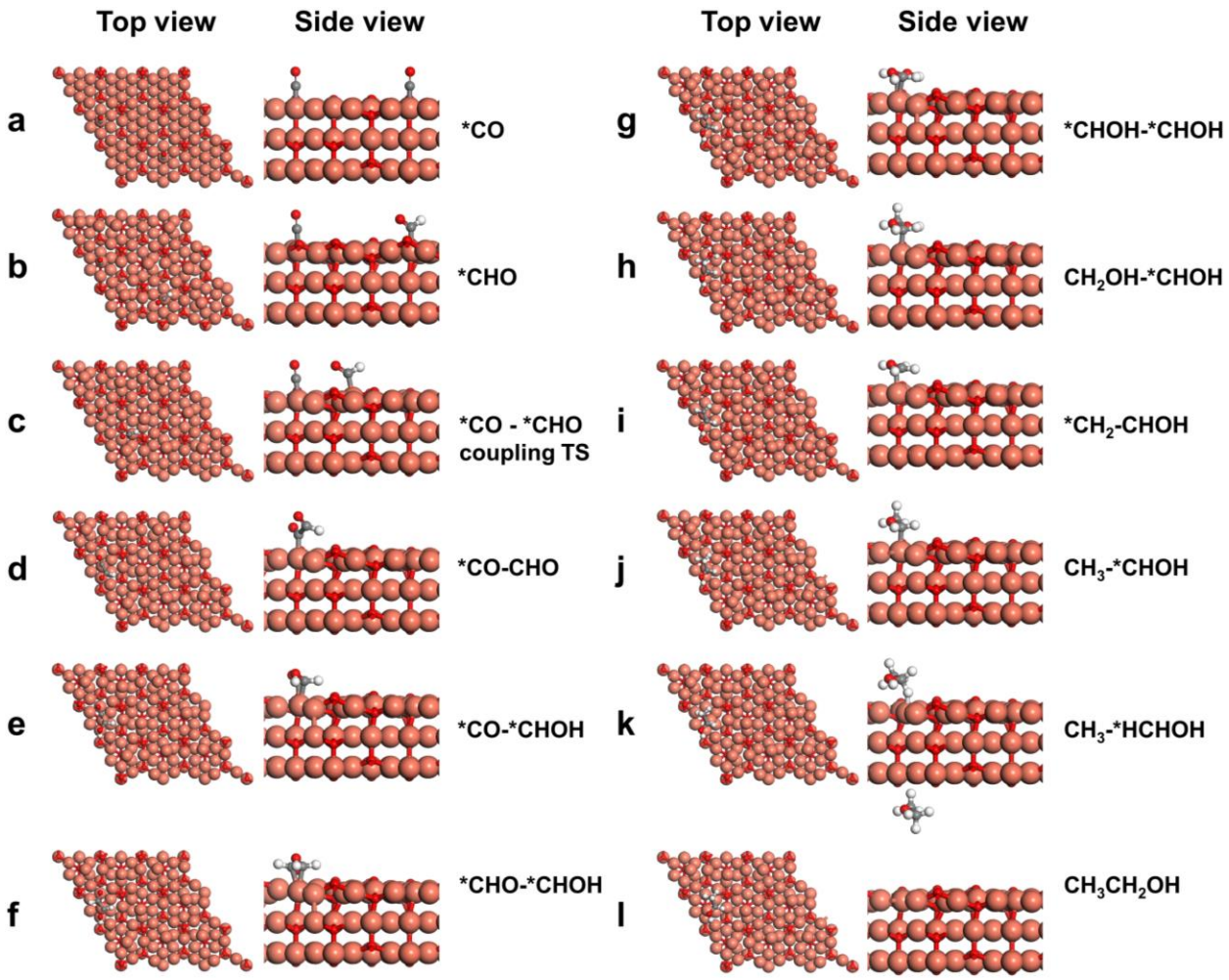

Fig. S29 Top and side views of different configurations for CO_2-to-CH_3CH_2OH conversion at low *CO coverage. (a to l) Top and side views of optimized adsorption configurations for main reaction intermediates during the overall PCRR to ethanol on Cu_2O (111) surface at low *CO coverage. The brown, gray, red, and white balls represent Cu, C, O, and H atoms, respectively. TS means transition state of C-C coupling. * represents surface adsorption.

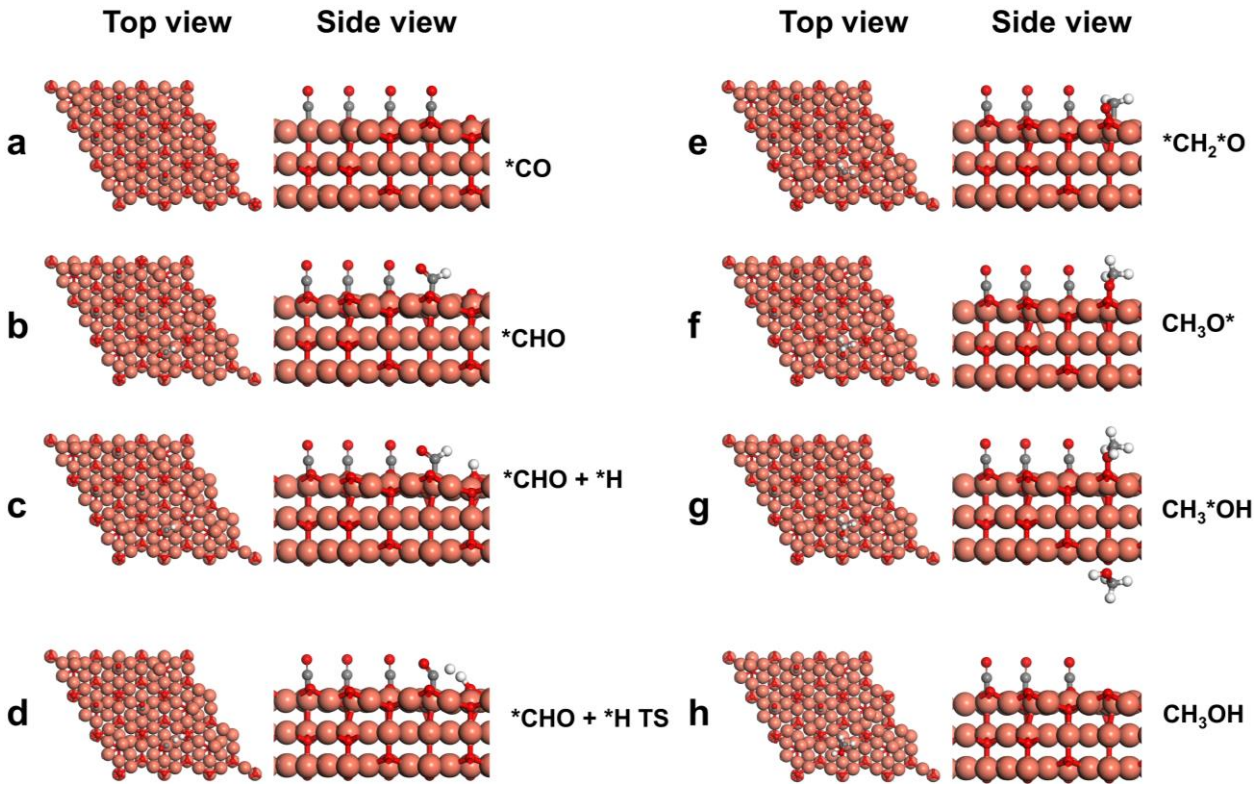

Fig. S30 Top and side views of different configurations for CO_2-to-CH_3OH conversion at high *CO coverage. (a to h) Top and side views of optimized adsorption configurations for main reaction intermediates during the overall PCRR to methanol on Cu_2O (111) surface at high *CO coverage. The brown, gray, red, and white balls represent Cu, C, O, and H atoms, respectively. TS means the transition state from *CHO to *CH_2O. * represents surface adsorption.

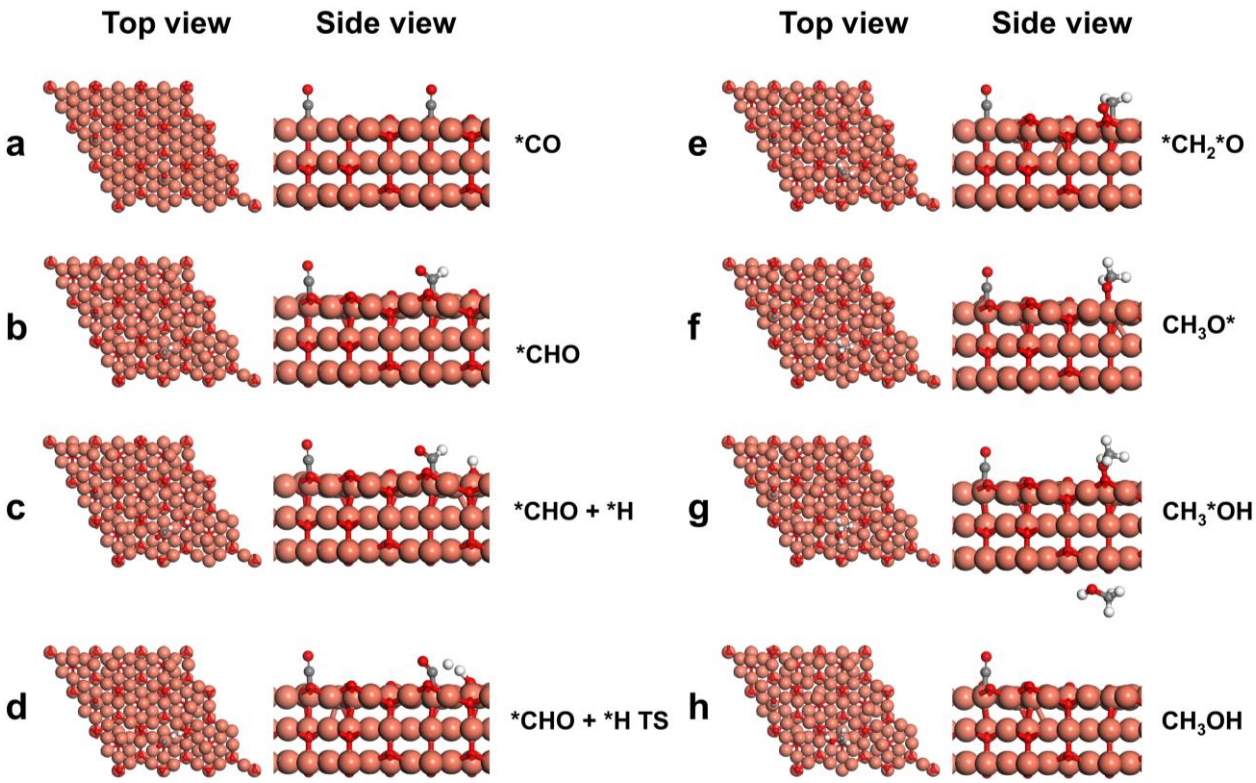

Fig. S31 Top and side views of different configurations for CO_2-to-CH_3OH conversion at low *CO coverage. (a to h) Top and side views of adsorption configurations of main reaction intermediates during the overall PCRR to methanol on Cu_2O (111) surface at low *CO coverage. The brown, gray, red, and white balls represent Cu, C, O, and H atoms, respectively. TS means the transition state from *CHO to *CH_2O. * represents surface adsorption.

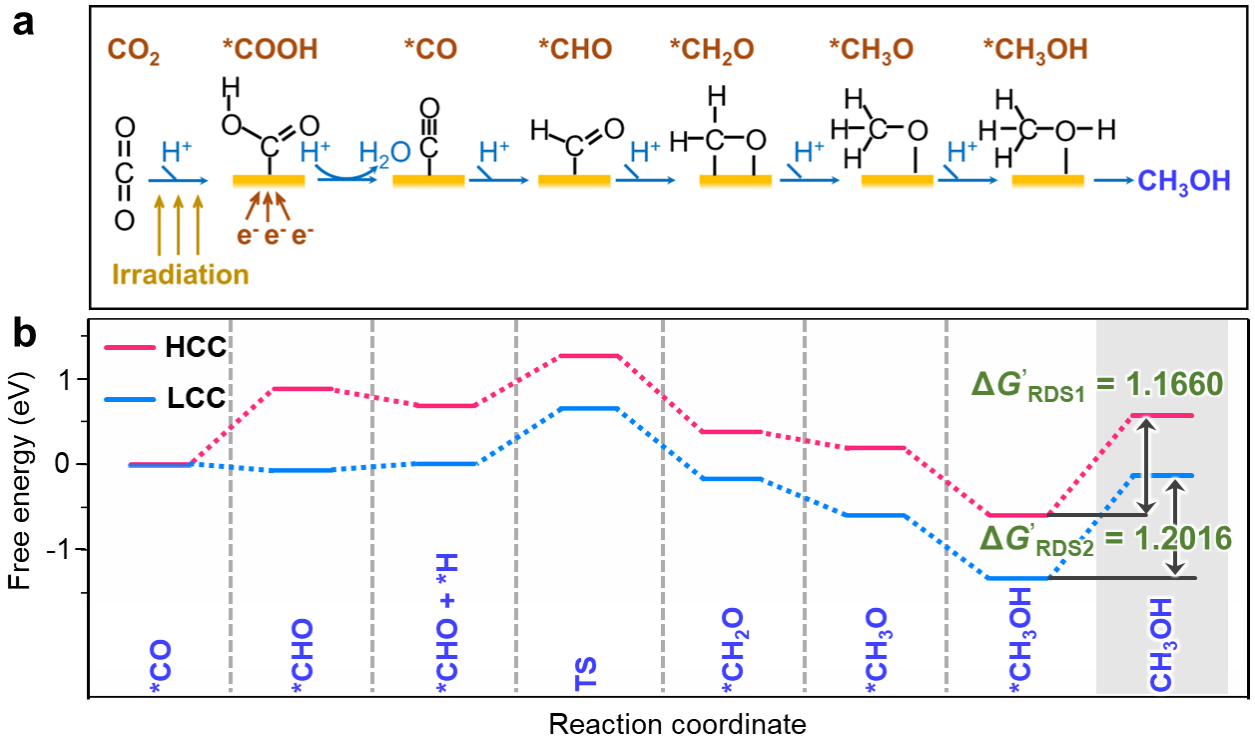

Fig. S32 Reaction mechanism of methanol formation. (a) Possible CO_2-to-methanol reaction pathway over the designed catalyst. (b) Gibbs free energy diagram of the methanol pathway on Cu_2O (111) surface at high *CO coverage (HCC) and low *CO coverage (LCC). ΔG_{RDS}' means the Gibbs free energy change for the rate-determining step of methanol formation. TS means the transition state from *CHO to *CH_2O. The *CH_3OH desorption step exhibits the highest energy barrier (denoted as ΔG_{RDS}'), making it the rate-determining step (RDS) for methanol formation. In comparison to the LCC state, the HCC state exhibits a lower ΔG_{RDS1}' with 1.1660 eV, which indicates that the enrichment of CO_2 on the catalyst surface also benefits methanol generation.

Table S1 Typical photocatalytic systems for CO_2 reduction to ethanol

Photocatalyst	Formation rate (μmol g^{-1} h^{-1})		Light source, reaction mode	Ref.
	Methanol	Ethanol		
O-CHS	**1073.04**	**996.18**	**Xe lamp (> 420 nm), Solid-liquid**	**This work**
Red phosphorus/Bi_2MoO_6	30.2	51.8	Xe lamp (> 400 nm), Solid-liquid	[22]
u-g-C_3N_4	6.3	4.51	Xe lamp (> 420 nm), Solid-liquid	[23]
m-g-C_3N_4	-	3.64	Xe lamp (> 420 nm), Solid-liquid	[23]
Monoclinic $BiVO_4$	-	101	Xe lamp (> 400 nm), Solid-liquid	[24]
Tetragonal $BiVO_4$	-	5.6	Xe lamp (> 400 nm), Solid-liquid	[24]
1 wt% Co-doped TiO_2	26	18	Halogen lamp (> 380 nm), Solid-vapor	[25]
Cu^{2+}-doped TiO_2	24	47	365 nm LED lamp, Solid-vapor	[26]
TiO_2	6.7	6.3	365 nm LED lamp, Solid-vapor	[26]
GO-TiO_2	12	145	Hg lamp, Solid-liquid	[27]
Rh nanowires/TiO_2	-	12.1	Xe lamp (< 400 nm), Solid-vapor	[28]
TiO_2-Pd nanowires	-	13	Xe lamp (< 400 nm), Solid-vapor	[28]
$NiO/Na_{1-x}La_xTaO_{3+x}$	60	19	Hg lamp (300-700 nm), Solid-liquid	[29]
MWCNTs/TiO_2(anatase)	-	29.9	UV lamp (365 nm), Solid-vapor	[30]
Cu_2O/ml-G	-	545	UV lamp (254 nm), Solid-liquid	[31]
Pt/TaON	-	2.03	Xe lamp (> 420 nm), Solid-liquid	[32]
$TiO_2/Ni(OH)_2$	0.58	0.37	Xe lamp (Simulated sunlight), Solid-vapor	[33]
1.5 wt%Ni^{2+}–TiO_2	5.58	13.2	Halogen and mercury lamp, Solid-vapor	[34]
5%GQDs/V-TiO_2	22.5	13.5	Xe lamp (Simulated sunlight), Solid-liquid	[35]
23.2% AgBr/TiO_2	77.87	13.28	Xe lamp (> 420 nm), Solid-liquid	[36]
ZnO/g-C_3N_4	19.0	2.5	Xe lamp (Simulated sunlight), Solid-liquid	[37]
Ag_3PO_4/g-C_3N_4	-	1.3	Xe lamp (Simulated sunlight), Solid-liquid	[38]
5.8wt%Pd/g-C_3N_4	-	2.18	Xe lamp (> 420 nm), Solid-vapor	[39]
Cu/Pt-$HCa_2Ta_3O_{10}$	7.4	113.2	Xe lamp (Simulated sunlight), Solid-vapor	[40]
$BiVO_4$/RGO	-	5.15	Xe lamp (Simulated sunlight), Solid-liquid	[41]
Ag@AgBr/CNT	17.21	2.94	Xe lamp (> 420 nm), Solid-liquid	[42]
Red Ag/AgCl	29.2	44.6	Xe lamp (> 420 nm), Solid-liquid	[43]
$Sr_3Ti_{(2-x-y)}Fe_xS_yO_{(7-z)}N_z$	60.1	9.9	Hg lamp (300-700 nm), Solid-liquid	[44]
$Zn_{0.8}Cd_{0.2}S$	2.5	6.0	Xe lamp (> 400 nm), Solid-liquid	[45]
Pd/Mn-TiO_2	0.104	5.699	Xe lamp (UV light), Solid-liquid	[46]
$Na_{(1-x)}La_xTaO_{(3+x)}$	35.0	3.1	Hg lamp (300-700 nm), Solid-liquid	[47]
CoTPP/$Na_{(1-x)}La_xTaO_{(3+x)}$	36.2	21.4	Hg lamp (300-700 nm), Solid-liquid	[47]
Cu SAs/UiO-66-NH_2	5.33	4.22	Xe lamp (400 nm), Solid-liquid	[48]
Trimodal silica/g-C_3N_4	-	90	Xe lamp (λ > 420 nm), Solid-liquid	[49]

Photocatalyst	Formation rate (μmol g^{-1} h^{-1})		Light source, reaction mode	Ref.
	Methanol	Ethanol		
g-C_3N_4 (Defect)	3.85	1.98	Xe lamp (λ > 420 nm), Solid-vapor	[50]
$Sn_xNb_{1-x}O_2$	5.25	130.36	Xe lamp, Solid-vapor	[51]
$SrTiO_3$(La Cr)/Cu @ Ni/TiN	-	21.3	Xe lamp, Solid-liquid	[52]
$Cu/Cd_{0.5}Zn_{0.5}S$	-	2.26 μmol/h	Xe lamp, Solid-liquid	[6]
Cu_2O/Pt/NH_2-MIL-125(Ti)	144.82	239.49	Xe lamp (400 nm), Solid-liquid	[53]
Cu_2O/g-C_3N_4	-	375.66	Xe lamp (> 420 nm), Solid-liquid	[54]
1.0 wt% AuCu/g-C_3N_4	-	211.9	Xe lamp (> 420 nm), Solid-liquid	[55]
Cu_2O-modified layered BiOI	152.26	68.49	Xe lamp, Solid-liquid	[56]
1%CeO_2/3%CuO/TiO_2	-	30.5	UV lamp (254 nm), Solid-liquid	[57]
InCu/PCN	-	28.5	Xe lamp, Solid-liquid	[58]
Pd_xIn_y@N_3-COF	24.605	8.645	Xe lamp (400 nm), Solid-liquid	[59]
Zn(II)/Cu(I, II)- 1,3,5-benzenetricarboxylic acid	4470	605	Xe lamp, Solid-liquid	[60]
$BiOI_xCl_y$	130.265	33.066	Xe lamp, Solid-liquid	[61]

Table S2 Fitted parameters obtained from decay curves of the samples

Sample	τ_1 (ns)	τ_2 (ns)	τ_3 (ns)	τ_a (ns)	χ^2
O-CHS	0.53	4.52	36.77	1.97	1.28
O-CNS	0.55	5.03	40.68	1.85	1.22
O-CSS	0.48	4.69	59.76	1.49	1.25

τ_1, τ_2 and τ_3 represent the lifetime (ns) in the radiative, non-radiative and energy transfer process, respectively.[62] τ_a represents the average lifetime (ns) of photogenerated carriers. χ^2 represents the goodness of fit parameter.

Table S3 BET surface areas and pore sizes of all samples

Sample	Surface area (cm^3 g^{-1})	Pore size (nm)
CHS	38.0891	12.8139
O-CHS	35.2125	11.3167
CSS	9.0563	18.9323
O-CSS	8.6979	17.2529
CNS	50.92	28.447
O-CNS	46.95	26.164

Table S4 Gibbs free energy change (ΔG) of CO adsorption on the Cu_2O (111) surface at different *CO coverages

*CO coverage	ΔG (eV)
high *CO coverage	-2.450
low *CO coverage	-2.398

Table S5 Different intermediates potentially formed with different numbers of H^+ transfers for ethanol generation at high *CO coverage

Number of H^+ transferred	Intermediate	Energy（eV）
1	CHO	-805.29535
	COH	-803.35949
	COCHOH	-808.62853
2	$COCH_2O$	-808.55206
	COHCHO	-808.01623
	CHOCHO	-808.25042
	CHOCHOH	-812.61667
3	$COCH_2OH$	-812.40418
	$COCH + H_2O$	-812.08371
	COHCHOH	-811.85635
	CHOHCHOH	-817.08981
4	$CHOCH_2OH$	-816.21638
	CH_2OCHOH	-815.88745
	$CHOCH + H_2O$	-815.44839
	$CH_2OHCHOH$	-820.14588
5	$CHOHCH_2OH$	-820.12281
	$CHOHCH + H_2O$	-819.41174
	$CHCHOH + H_2O$	-819.24416
	$CH_2CHOH + H_2O$	-824.7696
6	$CH_3OHCHOH$	-823.5143
	CH_2OHCH_2OH	-823.97908
	$CH_2OHCH + H_2O$	-822.48591
	CH_3CHOH	-813.61466
7	CH_2CH_2OH	-813.43481
	$CH_2CH + H_2O$	-812.60829

In a series of continuous H^+ transfer processes, different hydrogenation positions are considered, and the state with the lowest energy is selected and marked in blue (as shown in Table S4). The initial step is the hydrogenation of *CO. It can be seen that the total energy required for adding one *H to the carbon atom of *CO to form *CHO, is lower than that for adding *H to the oxygen of *CO to form *COH. Therefore, *CHO is considered the result of *CO hydrogenation. Subsequently, *CO-*CHO coupling occurs and the hydrogenation processes continue. The different situations of the hydrogenation of *CO-*CHO illustrate that *COCHOH is the state with the lowest energy. Similarly, *CHOCHOH, *CHOHCHOH, *CH_2OHCHOH, *CH_2CHOH, and *CH_3CHOH are the results of a series of cascading hydrogeneration reactions.

Table S6 Different intermediates potentially formed with different numbers of H^+ transfers for ethanol generation at low *CO coverage

Number of H^+ transferred	Intermediate	Energy（eV）
1	CHO	-772.54737
	COH	-770.28191
	COCHOH	-775.72891
2	$COCH_2O$	-775.69805
	COHCHO	-775.44682
	CHOCHO	-775.38418

Number of H^+ transferred	Intermediate	Energy（eV）
3	CHOCHOH	-779.74153
	$COCH_2OH$	-779.66037
	COCH + H_2O	-779.23103
	COHCHOH	-778.82308
4	CHOHCHOH	-784.22011
	$CHOCH_2OH$	-783.28004
	CH_2OCHOH	-783.26036
	CHOCH + H_2O	-781.78617
5	$CH_2OHCHOH$	-787.22776
	$CHOHCH_2OH$	-787.1894
	CHOHCH + H_2O	-786.53899
	CHCHOH + H_2O	-786.26208
6	CH_2CHOH + H_2O	-791.88701
	$CH_3OHCHOH$	-791.37778
	CH_2OHCH_2OH	-791.21733
	CH_2OHCH + H_2O	-789.58538
7	CH_3CHOH	-780.716
	CH_2CH_2OH	-780.51346
	CH_2CH + H_2O	-779.70392

The optimal hydrogenation results for the ethanol pathway at low *CO coverage are similar to those at high *CO coverage, as shown in Table S5, highlighted in blue.

Table S7 Different intermediates potentially formed with different numbers of H^+ transfers for methanol generation at high *CO coverage

Number of H^+ transferred	Intermediate	Energy（eV）
1	CHO	-805.29535
	COH	-803.35949
2	CH_2O	-809.35756
	CHOH	-808.78468
3	CH_3O	-813.23303
	CH_2OH	-813.00428

In a series of continuous H^+ transfer processes, different hydrogenation positions are considered, and the state with the lowest energy is selected and marked in blue (as shown in Table S6). The initial step involves the hydrogenation of *CO. It can be seen that the total energy for adding one *H to the carbon atom of *CO to form *CHO, is lower than that for adding *H to the oxygen of *CO to form *COH. Therefore, *CHO is considered the result of *CO hydrogenation. Subsequently, the hydrogenation of *CHO continues. The different situations of *CHO hydrogenation illustrate that *CH_2O is the state with the lowest energy. Likewise, *CH_3O is the result of the subsequent hydrogeneration step.

Table S8 Different intermediates potentially formed with different numbers of H^+ transfers for methanol generation at low *CO coverage

Number of H^+ transferred	Intermediate	Energy（eV）
1	CHO	-772.54737
	COH	-770.28191
2	CH_2O	-776.45335
	CHOH	-775.8547
3	CH_3O	-780.4859
	CH_2OH	-780.39353

The optimal hydrogenation results for the methanol pathway at low *CO coverage are similar to those at high *CO coverage and are displayed in Table S7, highlighted in blue.

Table S9 Possible reaction pathway during the overall PCRR to ethanol on the catalyst

Ethanol reaction pathway
$CO_2 + e^- \rightarrow CO_2^-$
$CO_2^- + H^+ + e^- \rightarrow *COOH$
$*COOH + H^+ + e^- \rightarrow *CO + H_2O$
$*CO + H^+ + e^- \rightarrow *CHO$
$*CO + *CHO + e^- \rightarrow *COCHO + *$
$*COCHO + H^+ + e^- \rightarrow *COCHOH$
$*COCHOH + H^+ + e^- \rightarrow *CHOCHOH$
$*CHOCHOH + H^+ + e^- \rightarrow *CHOHCHOH$
$*CHOHCHOH + H^+ + e^- \rightarrow *CH_2OHCHOH$
$*CH_2OHCHOH + H^+ + e^- \rightarrow *CH_2CHOH + H_2O$
$*CH_2CHOH + H^+ + e^- \rightarrow *CH_3CHOH$
$*CH_3CHOH + H^+ + e^- \rightarrow *CH_3CH_2OH$
$*CH_3CH_2OH \rightarrow CH_3CH_2OH\ (g) + e^- + *$

Table S10 Possible reaction pathway during the overall PCRR to methanol on the catalyst

Methanol reaction pathway
$CO_2 + e^- \rightarrow CO_2^-$
$CO_2^- + H^+ + e^- \rightarrow *COOH$
$*COOH + H^+ + e^- \rightarrow *CO + H_2O$
$*CO + H^+ + e^- \rightarrow *CHO$
$*CHO + H^+ + e^- \rightarrow *CH_2O$
$*CH_2O + H^+ + e^- \rightarrow *CH_3O$
$*CH_3O + H^+ + e^- \rightarrow *CH_3OH$
$*CH_3OH \rightarrow CH_3OH\ (g) + e^- + *$

Table S11 Thermochemical data of the reactants and products for the overall PCRR

Compound	Chemical formula	$\Delta_f G_i^{\ominus}$ (kJ mol^{-1})
Ethanol	CH_3CH_2OH	-174.8

Compound	Chemical formula	$\Delta_f G_i^{\ominus}$ (kJ mol^{-1})
Carbon dioxide	CO_2	-394.4
Oxygen	O_2	0
Water	H_2O	-237.1

References

1 H. Liu and G. Cao, *Sci Rep*, 2016, **6**, 23936.
2 J. Mo, J. Sha, D. Li, Z. Li and Y. Chen, *Nanoscale*, 2019, **11**, 8408-8415.
3 J. Li, G. Chen, Y. Zhu, Z. Liang, A. Pei, C.-L. Wu, H. Wang, H. R. Lee, K. Liu, S. Chu and Y. Cui, *Nat. Catal.*, 2018, **1**, 592-600.
4 W. M. Haynes, *CRC handbook of chemistry and physics*, CRC, 2016.
5 R. T. Rashid, Y. Chen, X. Liu, F. A. Chowdhury, M. Liu, J. Song, Z. Mi and B. Zhou, *Proc. Natl. Acad. Sci. U. S. A.*, 2022, **119**, e2121174119.
6 S. Bai, H. Qiu, M. Song, G. He, F. Wang, Y. Liu and L. Guo, *eScience*, 2022, **2**, 428-437.
7 Y. A. Wu, I. McNulty, C. Liu, K. C. Lau, Q. Liu, A. P. Paulikas, C.-J. Sun, Z. Cai, J. R. Guest, Y. Ren, V. Stamenkovic, L. A. Curtiss, Y. Liu and T. Rajh, *Nat. Energy*, 2019, **4**, 957-968.
8 P.-L. Wang, W. Zhang, Q. Yuan, T. Mai, M.-Y. Qi and M.-G. Ma, *J. Colloid Interface Sci.*, 2023, **645**, 306-318.
9 H. Perschke and E. Broda, *Nature*, 1961, **190**, 257-258.
10 P. Zhang, T. Wang, X. Chang, L. Zhang and J. Gong, *Angew. Chem. Int. Ed.*, 2016, **128**, 5945-5949.
11 Y. Kuwahara, J. Aoyama, K. Miyakubo, T. Eguchi, T. Kamegawa, K. Mori and H. Yamashita, *J. Catal.*, 2012, **285**, 223-234.
12 C. Gao, Z. Sun, K. Li, Y. Chen, Y. Cao, S. Zhang and L. Feng, *Energ. Environ. Sci.*, 2013, **6**, 1147-1151.
13 Z. Li, N. Xiong and G. Gu, *Dalton Trans.*, 2018, **48**, 182-189.
14 H. Yu, S. Qu, P. R. Chen, K. Q. Ou, J. Y. Lin, Z. H. Guo, L. Zheng, J. K. Li, S. Huang, Y. Teng, L. Zou and J. L. Song, *J. Hazard. Mater.*, 2022, **430**, 128351.
15 X. Liu, L. Cao, W. Sun, Z. Zhou and J. Yang, *Res. Chem. Intermed.*, 2016, **42**, 6289-6300.
16 Z. He, J. Fu, B. Cheng, J. Yu and S. Cao, *Appl. Catal. B*, 2017, **205**, 104-111.
17 M. P. r. S. Gonza´lez, M. Barrera, A. R. Gonza´lez Elipe, and R. M. Souto, *J. Phys. Chem. B*, 1998, **102**, 5483-5489.
18 C. Y. Toe, J. Scott, R. Amal and Y. H. Ng, *J. Photoch. Photobio. C*, 2019, **40**, 191-211.
19 R. D. Zhonghai Zhang, Lianbin Zhang, Haibo Zhu, Hongnan Zhang, and Peng Wang, *ACS Nano*, 2013, **7**, 1709-1717.
20 C. Y. Toe, Z. Zheng, H. Wu, J. Scott, R. Amal and Y. H. Ng, *Angew. Chem. Int. Ed.*, 2018, **57**, 13613-13617.
21 Y. Xia, K. Xiao, B. Cheng, J. Yu, L. Jiang, M. Antonietti and S. Cao, *ChemSusChem*, 2020, **13**, 1730-1734.
22 R. Das, K. Das, B. Ray, C. P. Vinod and S. C. Peter, *Energ. Environ. Sci.*, 2022, **15**, 1967-1976.
23 J. Mao, T. Peng, X. Zhang, K. Li, L. Ye and L. Zan, *Catal. Sci. Technol.*, 2013, **3**, 1253-1260.
24 Y. Liu, B. Huang, Y. Dai, X. Zhang, X. Qin, M. Jiang and M.-H. Whangbo, *Catal. Commun.*, 2009, **11**, 210-213.
25 O. Ola and M. M. Maroto-Valer, *Appl. Catal. A*, 2015, **502**, 114-121.
26 M. Cheng, S. Yang, R. Chen, X. Zhu, Q. Liao and Y. Huang, *Int. J. Hydrogen Energy*, 2017, **42**, 9722-9732.
27 L. Pastrana-Martínez, A. Silva, N. Fonseca, J. Vaz, J. Figueiredo and J. Faria, *Top. Catal.*, 2016, **59**, 1279-1291.
28 Y. Zhu, Z. Xu, Q. Lang, W. Jiang, Q. Yin, S. Zhong and S. Bai, *Appl. Catal. B*, 2017, **206**, 282-292.
29 V. Jeyalakshmi, R. Mahalakshmy, K. R. Krishnamurthy and B. Viswanathan, *Catal. Today*, 2016, **266**, 160-167.
30 X.-H. Xia, Z.-J. Jia, Y. Yu, Y. Liang, Z. Wang and L.-L. Ma, *Carbon*, 2007, **45**, 717-721.
31 L. Hurtado, R. Natividad and H. García, *Catal. Commun.*, 2016, **84**, 30-35.
32 Q. Han, Y. Zhou, L. Tang, P. Li, W. Tu, L. Li, H. Li and Z. Zou, *RSC Adv.*, 2016, **6**, 90792-90796.
33 A. Meng, S. Wu, B. Cheng, J. Yu and J. Xu, *J. Mater. Chem. A*, 2018, **6**, 4729-4736.
34 O. Ola and M. M. Maroto-Valer, *J. Catal.*, 2014, **309**, 300-308.
35 J.-P. Zou, D.-D. Wu, J. Luo, Q.-J. Xing, X.-B. Luo, W.-H. Dong, S.-L. Luo, H.-M. Du and S. L. Suib, *ACS Catal.*, 2016, **6**, 6861-6867.
36 M. Abou Asi, C. He, M. Su, D. Xia, L. Lin, H. Deng, Y. Xiong, R. Qiu and X.-z. Li, *Catal. Today*, 2011, **175**, 256-263.
37 Y. He, Y. Wang, L. Zhang, B. Teng and M. Fan, *Appl. Catal. B*, 2015, **168**, 1-8.
38 Y. He, L. Zhang, B. Teng and M. Fan, *Environ. Sci. Technol.*, 2015, **49**, 649-656.
39 S. Bai, X. Wang, C. Hu, M. Xie, J. Jiang and Y. Xiong, *Chem. Commun.*, 2014, **50**, 6094-6097.
40 N.-N. Vu, C.-C. Nguyen, S. Kaliaguine and T.-O. Do, *Adv. Sustainable Syst.*, 2017, **1**, 1700048.
41 A. Wang, S. Shen, Y. Zhao and W. Wu, *J. Colloid Interface Sci.*, 2015, **445**, 330-336.
42 M. Abou Asi, L. Zhu, C. He, V. K. Sharma, D. Shu, S. Li, J. Yang and Y. Xiong, *Catal. Today*, 2013, **216**, 268-275.
43 B. Cai, J. Wang, S. Gan, D. Han, Z. Wu and L. Niu, *J. Mater. Chem. A*, 2014, **2**, 5280-5286.
44 V. Jeyalakshmi, R. Mahalakshmy, K. R. Krishnamurthy and B. Viswanathan, *Catal. Today*, 2018, **300**, 152-159.
45 L. Tang, L. Kuai, Y. Li, H. Li, Y. Zhou and Z. Zou, *Nanotechnology*, 2018, **29**, 064003.
46 T. Peng, K. Wang, S. He, X. Chen, W. Dai and X. Fu, *Catal. Sci. Technol.*, 2021, **11**, 2261-2272.
47 V. Jeyalakshmi, S. Tamilmani, R. Mahalakshmy, P. Bhyrappa, K. R. Krishnamurthy and B. Viswanathan, *J. Mol. Catal. A: Chem.*, 2016, **420**, 200-207.
48 G. Wang, C. T. He, R. Huang, J. Mao, D. Wang and Y. Li, *J. Am. Chem. Soc.*, 2020, **142**, 19339-19345.
49 Y. Wang, H. Jia, H. Gong, L. Zhou, Z. Qiu, X. Fang and T. Du, *Chem. Eng. J.*, 2021, **426**, 130877.
50 P. Xia, M. Antonietti, B. Zhu, T. Heil, J. Yu and S. Cao, *Adv. Funct. Mater.*, 2019, **29**, 1900093.
51 S. Gao, H. Guan, H. Wang, X. Yang, W. Yang and Q. Li, *J. Adv. Ceram.*, 2022, **11**, 1404-1416.
52 H. Yu, C. Sun, Y. Xuan, K. Zhang and K. Chang, *Chem. Eng. J.*, 2022, **430**, 132940.
53 Q. Jia, J. Zhou, L. Gong, L. Wang, X. Ma and Y. Zhao, *Mol. Catal.*, 2022, **530**, 112599.
54 P. Li, L. Liu, W. An, H. Wang and W. Cui, *Appl. Surf. Sci.*, 2021, **565**, 150448.
55 P. Li, L. Liu, W. An, H. Wang, H. Guo, Y. Liang and W. Cui, *Appl. Catal. B*, 2020, **266**, 118618.
56 J. Cai, Y. Xiao, Y. Tursun and A. Abulizi, *Mater. Sci. Semicond. Process.*, 2022, **149**, 106891.
57 P. Seeharaj, N. Vittayakorn, J. Morris and P. Kim-Lohsoontorn, *Nanotechnology*, 2021, **32**, 375707.
58 H. Shi, H. Wang, Y. Zhou, J. Li, P. Zhai, X. Li, G. G. Gurzadyan, J. Hou, H. Yang and X. Guo, *Angew. Chem. Int. Ed.*, 2022, **61**, e202208904.
59 Y. Huang, P. Du, W.-X. Shi, Y. Wang, S. Yao, Z.-M. Zhang, T.-B. Lu and X. Lu, *Appl. Catal. B*, 2021, **288**, 120001.

60 K. Wu, C. Liu, Y. Chen, H. Jiang, Q. Peng, Y. Chen, D. Fang, B. Shen, Q. Wu, L. Zhan, W. Sun, W. Di and H. Sun, *Appl. Catal. A*, 2023, **650**, 118970.
61 H. Fu, T. Zhang, A. Abulizi, K. Okitsu and Y. Tursun, *J. Ind. Eng. Chem.*, 2023, **117**, 510-521.
62 F. Xu, K. Meng, B. Cheng, S. Wang, J. Xu and J. Yu, *Nat. Commun.*, 2020, **11**, 4613.